Formation of mineral-associated organic matter via rock weathering: an experimental test for the organo-metallic glue hypothesis

Kaori Matsuoka[1], Jo Jinno[1], Hiroaki Shimada[2], Emi Matsumura[1], Ryo Shingubara[3], Puu-Tai Yang[1], Rota Wagai[1]

[1]Institute for Agro-Environmental Sciences, National Agriculture and Food Research Organization, Tsukuba, 305-8604, Japan

[2]Division of Plant Production Science, Section of Plant Production Science Research Center for Global Agromedicine, Obihiro University of Agriculture and Veterinary Medicine, Obihiro, 080-8555, Japan

[3]Research Center for Advanced Analysis, National Agriculture and Food Research Organization, Tsukuba, 305-8604, Japan

Correspondence: Kaori Matsuoka (matsuoka.kaori811@naro.go.jp; kaori.matsuoka@hotmail.co.jp); Rota Wagai (wagai.rota200@naro.go.jp; rota.wagai@gmail.com)

Abstract. Mineral-associated organic matter, the dominant form of relatively stable carbon (C) in soil, often co-occurs with reactive iron (Fe) and aluminum (Al) phases across soils. Yet, how organo-metallic associations at the molecular scale give rise to emergent soil properties such as aggregate formation and the persistence of organic matter (OM) in soil remains unclear. The organo-metallic glue hypothesis proposes that dissolved metal released from weathering and microbially processed OM form cohesive organo-metallic phases that bind other particles into stable assemblages. We tested this concept using an artificial soil system comprising crushed rocks (fine basalt: 20–38 μm, coarse basalt and granite: 38–75 μm, and river sand), mixed with leaf compost and microbial inoculum, subjected to eight wet-dry cycles using artificial rainwater (pH 4.7) over 55 days. Sequential density fractionation after the incubation revealed the formation of meso-density, organo-mineral assemblages (1.8–2.4 g cm^{-3}: MF) in the following order: fine basalt > coarse basalt > granite > sand. The accretion of C and oxalate-extractable Fe, Al, and Si in MF generally followed the same pattern. Fine basalt showed the strongest increase in extractable metals, especially Fe, in MF and the highest leaching of Fe and base cations (esp. Na and Ca). Enrichment of extractable Fe, Al, and Si in MF and their slight depletion from high-density fraction (> 2.4 g cm^{-3}) suggest that weathering-derived metals first associated with OM, forming organo-metal rich phases that subsequently bound other particles to form organo-mineral assemblages. MF formed in fine basalt treatment had the C:(Fe+Al) molar ratio of 0.6, consistent with organo-metal coprecipitates. Preferential incorporation of microbially-processed, N-rich OM into MF in the two basalt treatments was indicated by lower C:N ratios by 23–25 units and enrichment of $\delta^{13}C$ and $\delta^{15}N$ by 0.9–1.2‰ and 0.6‰, respectively, relative to low-density fraction (< 1.8 g cm^{-3}). SEM and STXM/NEXAFS analyses of limited MF materials confirmed the presence of shaking-resistant microaggregates and the co-localization of microbially altered C with Fe and Al. Collectively, these results provide experimental evidence supporting the organo-metallic glue hypothesis and demonstrate that basaltic rock weathering can rapidly promote organo-mineral assemblage formation. This mechanism links microbial processing, mineral weathering, and reactive metal dynamics, offering insights into early pedogenesis and soil OM formation under rock amendment conditions.

1 Introduction

Organic matter (OM) in soil plays a fundamental role in global carbon cycling, soil fertility, and ecosystem functioning (Lehmann et al., 2020; Friedlingstein et al., 2022; Angst et al., 2023). Its long-term persistence strongly depends on its physicochemical associations with reactive minerals such as aluminosilicate clays and iron (Fe) and aluminum (Al) oxides with high surface area and reactivity (e.g., Sørensen, 1972; Baldock and Skjemstad, 2000; Wattel-Koekkoek et al., 2003;

Saidy et al., 2015; Hemingway et al., 2019). Among these, pedogenic Fe-, Al-, and Si-bearing phases, formed during mineral weathering, are especially reactive. They occur as organo-metal complexes, short-range-ordered (SRO) aluminosilicates and metal oxides, and, to a less extent, crystalline metal oxides (e.g., Harter and Naidu, 1995; Cornell and Schwertmann, 2003; Parker, 2005; Ashida et al., 2021; Watanabe et al., 2023).

At larger scales, soils rich in pedogenic metals generally store more OM. For instance, basaltic and andesitic soils often accumulate greater OM stocks than granitic soils (Orgill et al., 2017; Angst et al., 2018; Rasmussen et al., 2005; Mao et al., 2020), while OM composition also exerts some control depending on ecosystem type and climate (Sollins et al., 1996; Hall et al., 2020). Pedogenic Fe and Al contents often correlate positively with soil OM stock and, to some extent, with C persistence inferred from radiocarbon analysis (e.g., Torn et al., 1997; Percival et al., 2000; Masiello et al., 2004; Lawrence et al., 2015; Shimada et al., 2022; von Fromm et al., 2025). Their protective effects on OM may persist even under decades of intensive cultivation in humid tropics (Arai et al., 2025). At the molecular scale, these metals form various associations with OM, including hydrophobic interactions, cation bridging, adsorption, organo-metal complexation, and coprecipitation, that enhance OM resistance to microbial degradation and dissolution (Keil and Mayer, 2014; Kleber et al., 2015). Recent spectroscopic studies revealed diverse modes of OM-mineral and OM-metal/metalloid associations. Those include coprecipitates of metal and metalloid oligomers with organics (Basile-Doelsch et al., 2015; Tamrat et al., 2018; Jamoteau et al., 2023; Jamoteau et al., 2025), calcium complexation (Rowley et al., 2023), and nanoscale organic layering on mineral surface (Possinger et al., 2020; Underwood et al., 2024). However, how these molecular-scale interactions give rise to emergent soil properties such as OM persistence and hierarchical aggregate/ pore structure remains a fundamental question (Asano and Wagai, 2014; Regelink et al., 2015; Rabot et al., 2018; Totsche et al., 2018; Yudina and Kuzyakov, 2023; Amelung et al., 2024). These hierarchical soil structures regulate microbial and plant root activities and thus link mineral reactivity to ecosystem functioning (Chorover et al., 2022; Hartmann and Six, 2023; Philippot et al., 2024).

The *organo-metallic glue* hypothesis (Wagai et al., 2020) provides a conceptual bridge between nanoscale mineral-organic interactions and macroscale aggregation, and may offer more mechanistic interpretation on previous observations (e.g., C protection within aggregates, C-metal correlations across bulk soils and physical fractions). It proposes that Fe and Al dissolved from minerals complex or coprecipitate with decomposing OM to form cohesive organo-metallic phases that act as "glue", binding mineral and organic particles into stable microaggregates. Support for this mechanism includes the consistent co-occurrence of extractable Fe and Al with nitrogen (N)-rich OM in meso-density fractions (1.8–2.4 g cm^{-3}) across diverse soils and the relatively constant OC:metal ratios among soil physical fractions within each soil (Wagai et al., 2020). Yet, testing this mechanism in natural soils is challenging because of their compositional heterogeneity and the influence of multiple pedogenic processes. An artificial soil system, which consists of defined mineral and OM components, would be suitable to assess specific mechanisms under controlled conditions. Previous experiments have shown that various mineral-organic associations can form rapidly (e.g., Vogel et al., 2014; Pronk et al., 2017; Bucka et al., 2021). However, their formation mechanisms remain poorly understood.

This study aimed to evaluate key aspects of the *organo-metallic glue* hypothesis using an artificial soil system composed of crushed rock and leaf compost. We hypothesized that the differences in rock weathering rate, and thus the supply rate of Fe and Al, govern the formation of organo-mineral assemblages in the presence of OM. To test this, we incubated two end-member igneous rocks (granite and basaltic rock) and quartz sand (as a control) with leaf compost and a soil inoculum, subjecting the rock-OM mixtures to weekly leaching-drying cycles for 55 days. Formation of organo-mineral assemblage was assessed via sequential density fractionation, elemental and extractable metal analyses, and, to a limited extent, microscopic characterization (SEM and STXM-NEXAFS). We expected meso-density fractions to show enrichment in extractable metals relative to low- and high-density fractions, reflecting the role of weathering-derived metals in binding OM into physically-stable microaggregates.

2 Materials and Methods

We prepared four types of rock-organic matter (OM) mixtures using crushed rock and river sand with leaf compost, followed by 55-day aerobic incubation with eight wet-dry cycles (Fig. 1). Microbial respiration was not measured. Lechates were collected for chemical composition. The mixtures after the incubation were destructively sampled and fractionated by density. Each fraction was analyzed for total C and N as well as extractable metals and metalloids. For selected samples and fractions, we also conducted microscopic/spectroscopic and microbial characterization.

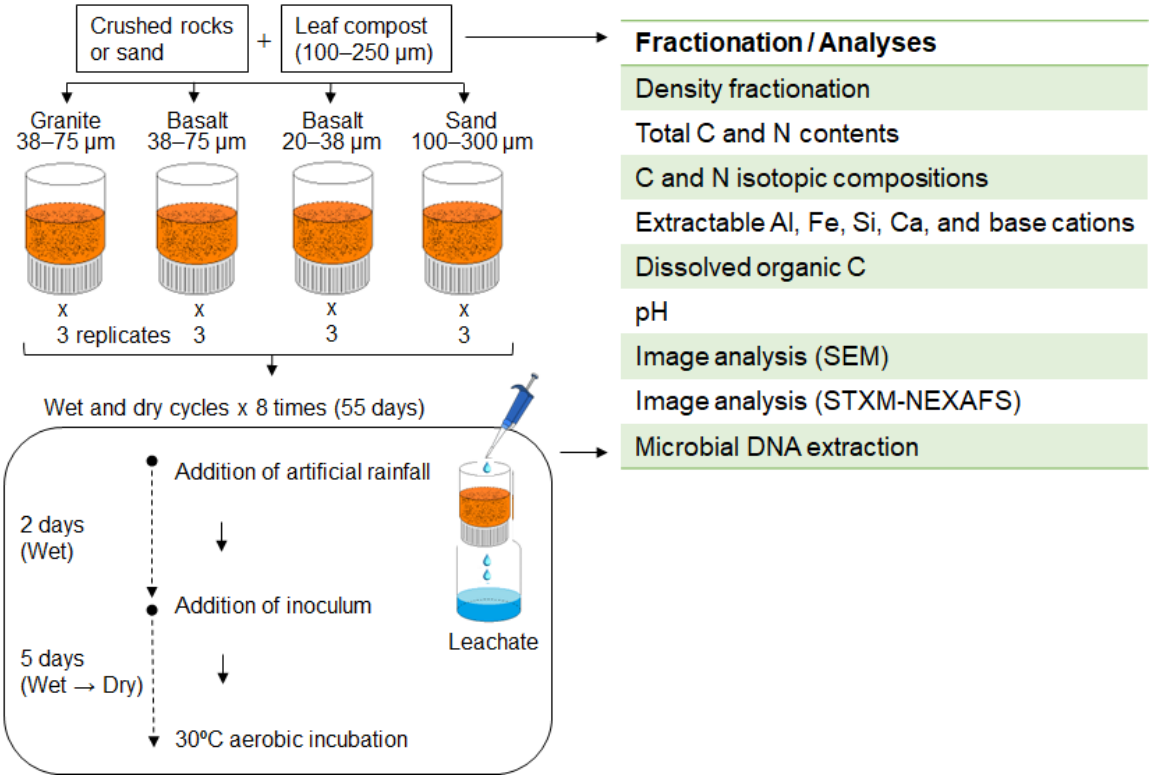

Figure 1. Schematics of the 55-day incubation experiment, including eight wet-dry cycles.

2.1 Source materials and rock-organic matter mixture preparation

We selected two rocks with contrasting chemical composition and weatherability, and a river sand as a low-reactivity control for comparison. Basalt, a mafic igneous rock, weathers faster and releases rock-forming elements including Fe and Al more rapidly than felsic granite due to the difference in silicate mineral composition. In addition to feldspars, basalt comprises minerals of lower degree of polymerization (e.g., pyroxene), whereas granite consists mainly of more-polymerized mineral (e.g., quartz) (Gray and Murphy, 2002; Chapman et al., 2009). Basaltic rock from Akita, Japan ("dust" type, < 2500 µm, Horie-Kenzai Co.) used in this study was mainly composed of plagioclase and pyroxene, with minor magnetite, olivine, smectite, and quartz (Fig. S1). The quartz detected likely resulted from the nearby lithologies. Further characterization of the basaltic rock sample is reported elsewhere (Yang et al., 2026). This rock is classified as basaltic andesite based on the Total Alkali-Silica diagram; however, for simplicity, the two particle-size treatments are referred to as "fine" and "coarse basalt". Granite used in this study was from Hiroshima, Japan ("pan" type, ≤ 75 µm, Yoko Bussan Co.) and had the elemental and mineralogical composition typical of granite (Table S1, Fig. S1).

These rocks were sorted for 38–75 µm and, additionally, for 20–38 µm (only basaltic rock). The source granite was ground in a blender (WB-1, Osaka Chemical Co., Japan) followed by wet sieving to isolate the 38–75 µm particle-size class. Coarse basalt (38–75 µm) was isolated by wet sieving. Fine basalt (20–38 µm) was isolated by repeated sedimentation of < 38 µm materials in deionized water until the supernatant was free of visible particles < 20 µm based on Stokes law.

Preferential loss of some fine-grain minerals (e.g., mica) and enrichment of coarser ones (e.g., quartz) during the sorting are possible. Mineralogical data, nevertheless, showed the size-sorted materials fall within a common compositional range (Fig. S1). River sand (mean particle size: 100–300 μm, Toyoura Keiseki Kogyo Co., Yamaguchi, Japan) served as a low-reactivity reference. All materials were oven-dried at 50 ºC. The elemental compositions of the four rock materials (granite, two sizes of basaltic rocks, and sand) were determined by X-ray fluorescence (NEX CG, Rigaku, Tokyo, Japan, Table S1). Mineralogy of granite and two basaltic rocks was identified by X-ray diffraction instrument equipped with a Cu tube (MiniFlex600-C, Rigaku, Tokyo, Japan, Fig. S1), scanned under XRF reduction mode from 3° to 90° (2θ) with a step size of 0.01°, at a speed of 5° min^{-1} (basaltic rock) and 10° min^{-1} (granite). The diffraction patterns were matched to the Crystallography Open Database. Smectite identified may include vermiculite because no phyllosilicate pre-treatment was applied. The two sizes of basaltic rock used in this study showed similar mineral composition to those reported in Yang et al. (2026). Particle size distributions (LA-920, Horiba Ltd., Kyoto, Japan) confirmed target ranges of the four rock materials (Fig. S2). The specific surface area (Table S2) was measured by N_2 gas sorption Autosorb iQ (Quantachrome Corp., Boynton Beach, FL, USA) using a multi-point BET approach (partial pressures of < 0.3) after outgassing under a vacuum at 150 °C. Total C concentration of the four rock materials was < 0.3 mg g^{-1}. This trace level of C derived more likely from organic matter (e.g., dust, microbial debris) rather than inorganic C because, at least for the basaltic rock, calcite was not detected by XRD and XANES analysis (Yang et al., 2026).

Leaf compost, the sole OM source, was produced mainly from tree leaves with one year of composting. Compost was air-dried, ground, and dry-sieved to a size of 100–250 μm. The compost had a C content of 408 mg g^{-1} with a C:N ratio of 41. The pH of the compost was 5.92 (H_2O) and 5.45 (KCl). The C structure of the compost had carbonyl-C 7.7%, aromatic-C 9.6%, O-alkyl-C 63.3%, and alkyl-C 19.4% (Fig. S3), which was assessed by solid-state ^{13}C nuclear magnetic resonance (NMR) spectrometry using an FT NMR system (JNM-ECA600II, JEOL Ltd., Tokyo, Japan) according to the procedure by Hiradate et al. (2004). The NMR spectrum was divided into chemical shift regions representative of the four major types of C present: 0–45 ppm (alkyl C), 45–110 ppm (O-alkyl C), 110–165 ppm (aromatic C), 165–210 ppm (carbonyl C) (Golchin et al., 1994). The total signal intensity and the proportion contributed by each C type were determined by the integration of the spectral regions.

The rock-OM mixtures were prepared by combining 20.00 g of each rock material with 2.50 g of the leaf compost under dry conditions in three replicates (Table S3). The rock-OM mixtures had an initial C content of 4.5%, comparable to C-rich cultivated topsoils. For the incubation experiment, the mixtures were placed in 50 mL plastic columns fitted with two layers of nylon mesh (≈ 6 μm) at the bottom.

2.2 Aerobic incubation with repeated leaching

The rock-OM mixtures were leached weekly with artificial rainwater over a 55-day experimental period. The rainwater composition was based on the typical Japanese precipitation data from the national acid deposition survey in 2014 (Horie et al., 2016): pH of 4.73 and contained the following ionic concentrations: SO_4^{2-} 18.1 μmol L^{-1}; NO_3^- 15.4 μmol L^{-1}; Cl^- 90.2 μmol L^{-1}; NH_4^+ 17.9 μmol L^{-1}; Na^+ 76.6 μmol L^{-1}; K^+ 2.62 μmol L^{-1}; Ca^{2+} 5.37 μmol L^{-1}; and Mg^{2+} 9.04 μmol L^{-1}. The solution was prepared using analytical-grade reagents: HCl, KCl, $CaCl_2$, $MgSO_47H_2O$, $NaNO_3$, $(NH_4)_2SO_4$, and NaCl.

The microbial inoculum was prepared from 0-5 cm surface soil of a long-term experimental field under no-till management with annual leaf compost input at the Institute for Agro-Environmental Sciences, Tsukuba, Japan (Wagai et al., 2013a). The same leaf compost served as the sole organic matter source for the rock-OM mixtures. The soil is classified as a Hydric Hapludand (Soil Survey Staff, 2014) and a Hydric-Silic Andosol (IUSS Working Group WRB, 2015). The microbial inoculum was produced by mixing field-moist soil with deionized water (1:15, w/v) and shaking the suspension with glass beads for 30 min. The mixture was then filtered through a 5-μm membrane filter (modified from Wagai and Sollins, 2002) to retain bacteria and fungal spores/fragments while removing major grazers. The inoculum was stored at 4 ºC for no longer

than 24 h before use.

The incubation started with 40 mL of rainwater applied to each column, left at room temperature overnight, and the leachate was collected. This weekly volume corresponded to Japan's mean annual precipitation assuming an even rainfall distribution (Horie et al., 2016). After leachate collection, 1 mL microbial inoculum was added. Water content was 52–63% on an air-dried basis (Table S4). The columns were then incubated in the dark at 30 ºC for 5 days until nearly complete drying, forming partially cemented material. Before re-wetting each time, the hardened material was gently loosened with a spatula to approximately half the column depth to facilitate infiltration of rainwater and inoculum. Subsequent cycles received 40 mL of rainwater and 0.1 mL of inoculum (reduced from 1 mL in the first cycle). Eight wet-dry cycles were completed in 55 days (Fig. 1). After incubation, the rock-OM mixtures were gently disaggregated, sieved (2 mm) using a spatula, homogenized in a plastic bag, and split for further analyses (Table S5). The leachates collected after each cycle were combined for each replicate and filtered for analyses of dissolved organic C (DOC), Al, Fe, Si, base cations (Na, Ca, K, and Mg), and pH.

2.3 Density fractionation before and after the incubation

The rock-OM mixtures after the incubation were fractionated by density with a moderate dispersion by mechanical shaking to distinguish organo-mineral assemblages as a meso-density fraction (1.8–2.4 g cm^{-3}; MF) from particulate OM as a low-density fraction (< 1.8 g cm^{-3}; LF) and crushed rock as a high-density fraction (> 2.4 g cm^{-3}; HF) as described in Wagai et al. (2015). Briefly, 10.0 g of the rock-OM mixture after the incubation were mixed with 30 mL of sodium polytungstate (SPT-0 grade, TC-Tungsten Compounds GmbH, D-96271 Grub am Forst, Germany) with a final density of 1.8 g cm^{-3} and shaken at 120 rpm for 30 min. The suspension was then centrifuged at 2330 *g* for 20 min, and the floating material was collected on a 0.45 μm membrane filter. These steps were repeated at least three times to maximize the recovery. The material on the filter was washed with deionized water until the electric conductivity was below 50 mS cm^{-1}; this operation produced the LF fraction. The residue was resuspended in SPT solution adjusted to 2.4 g cm^{-3} at the sample: extractant ratio of 10 g:30 mL, shaken, and centrifuged. The floating material (1.8–2.4 g cm^{-3}) was transferred to a 250 mL centrifuge bottle, mixed with deionized water, and centrifuged at 17,000 *g* for 20 min. The supernatant was decanted, and this rinsing step was repeated until the electric conductivity of the supernatant became < 50 mS cm^{-1}. The final material was recovered as the MF fraction of 1.8–2.4 g cm^{-3}. The remaining residue (> 2.4 g cm^{-3}) was rinsed with deionized water in the same way as above to isolate the HF fraction of > 2.4 g cm^{-3}. Recovered LF was oven-dried at 80 ºC, and MF and HF were freeze-dried. The materials recovered in MF by this operation are, therefore, organo-mineral aggregates that are physically resistant to the disruptive forces from the fractionation steps (esp. repeated mechanical shaking).

The initial four rock materials were fractionated at a density of 2.4 g cm^{-3} to distinguish MF and HF. Assuming that the initial leaf compost entirely consists of LF, we calculated C, N, and extractable Al, Fe, Si levels in each fraction for the rock-OM mixtures on Day 0. Masses recovered in each density fraction from the rock-OM mixtures on Day 0 and Day 55 are shown in Table S6.

2.4 Chemical analyses of the mixtures

Total C and N contents in the density fraction were determined by an elemental analyzer (vario MAX cube, Elementar Analysensysteme GmbH, Langenselbold, Germany). The degree of microbial alteration of OM can be assessed by C and N isotopic compositions (e.g., Sollins et al., 2009). Thus, initial leaf compost and density fractions under the two basalt treatments after the incubation were analyzed by a continuous-flow stable isotope mass spectrometer (Delta V Advantage, Thermo Fisher Scientific Inc., USA) coupled with an elemental analyzer (Flash EA 1112 Series). To minimize the N blank, a gas-tight automatic sampler was used (Zero Blank Autosampler, Costech Analytical Technologies Inc., USA). To increase the sensitivity for analyzing the N isotopes, the combustion and reduction tubes (both 18 mm outer diameters) were

exchanged with thinner ones (18–10 mm and 10–6 mm outer diameters, respectively; Ogawa et al., 2010; Koba et al., 2021). The obtained $^{13}C/^{12}C$ and $^{15}N/^{14}N$ ratios are shown in terms of the δ value ($\delta^{13}C$ and $\delta^{15}N$) relative to Vienna Pee Dee Belemnite and the air dinitrogen, respectively. Their analytical precisions are ± 0.2‰ except for the $\delta^{15}N$ values of the HF (± 0.4‰).

Extractable Al, Fe, Si, and Ca in the density fraction and bulk samples were quantified by the sequential extraction with sodium pyrophosphate (PP), oxalate-extractable (OX), and dithionite-extractable (DC), as described in Wagai et al. (2018). These extractions have been widely used as a practical method to estimate the concentrations of organo-metal complexes, short-range-ordered minerals, and pedogenic Fe oxides, respectively (Shang and Tiessen, 1998; Heckman et al., 2018; Ashida et al., 2021; Hall and Thompson, 2022). However, cautions are required for their interpretation due to the limited selectivity in extracting target phases as discussed previously (Wagai et al., 2013b; Rennert, 2019; Fukumasu et al., 2025). Briefly, each sample was extracted with 0.1 M sodium pyrophosphate (pH 10) at a sample: extractant ratio of 0.1 g:10 mL at 120 rpm for 16 h at room temperature, followed by high-speed centrifugation at 29,000 *g* for 40 min. After collecting an aliquot of the extract (approximately 7 mL) and discarding the remaining supernatant, the residue was extracted with 10 mL of 0.2 M acidified sodium oxalate solution (pH 3) at 150 rpm for 4 h at 25 ºC in the dark and centrifuged in the same way. After collecting an aliquot of the extract and discarding the remaining supernatant, the residue was added 0.167 g of sodium dithionite and then extracted with 10 mL of 0.646 M sodium citrate at 120 rpm for 16 h at room temperature and centrifuged in the same way.

The amounts of Al, Fe, Si, and base cations (Na, Ca, K, and Mg) after each of the three extractions were measured by an inductively coupled plasma optical emission spectrometer (700 series ICP-OES, Agilent Technologies, Inc., CA, United States). The combined leachate from the eight wet-dry cycles for each column of all four treatments was also analyzed in the same way. The leachate was also analyzed for DOC by a TOC analyzer (TOC-L, Shimadzu, Kyoto, Japan) using non-pergeable organic C mode and for pH.

The pH of the bulk samples from all four treatments after the incubation was measured using a glass electrode in ultra-pure water (0.4 g: 4 mL) after 1 h of shaking at 150 rpm. Subsequently, we added 1.6 mL of 3.5 M KCl to the water suspension to measure pH in the 1 M KCl conditions.

2.5 Imaging analyses of selected samples

Microscopic observation of the initial crushed rocks (granite, coarse basalt, and fine basalt) as well as the MF of their mixtures after the incubation was done using a scanning electron microscope (SU1510, Hitachi High-Tech Corporation, Tokyo, Japan). The subsets of MFs (stored in a suspension at ca 5 ºC after the density fractionation without freeze-drying) were diluted in ultra-pure water and deposited on a carbon tape, air-dried, and coated with palladium before the observation.

The subsets of MF from selected treatments (granite and coarse basalt) were assessed to examine the spatial arrangement of C, Al, and Fe, as well as C functional group within the meso-density materials (largely present as shaking-resistant microaggregates) in MF using scanning transmission X-ray microscopy (STXM) and near-edge X-ray absorption fine structure (NEXAFS). Another subset of suspended MF was diluted with ultra-pure water and weakly sonicated (< 10 J mL^{-1}) followed by deposition on a Si_3N_4 window (50 nm thick, window size 500 μm). To minimize the re-aggregation on the Si_3N_4 window upon drying, the samples were slowly dried at room temperature. Carbon, Al, and Fe were recorded by a compact STXM at BL-19A beamline in the Photon Factory of the High Energy Accelerator Research Organization, Ibaraki, Japan (Takeichi et al., 2016). The STXM data analysis was carried out with the IDL package aXis 2000 (Hitchcock, 2023). The distribution maps of C, Al, and Fe were obtained by subtracting the post-edge optical density (OD) image from the pre-edge OD image, respectively. Specifically, we collected images in the X-ray energy region of 280.0 and 300.0 eV for C K-edge adsorption, 700 and 709.5 eV for Fe L-edge adsorption, and 1550.0 and 1567.0 eV for Al K-edge adsorption (Solomon et al., 2012). The spatial resolution of the images was 200 nm. Deposited materials inevitably have sample thickness variation.

Interpretation of the spectral results therefore requires cautions because the obtained signal from each pixel is intensified in the thicker region of the deposited sample (Wan et al., 2007).

2.6 Microbial community analyses

Bacteria may exert stronger control on rock weathering than fungi under our short-term conditions with repeated physical mixing. We thus assessed the changes in bacterial community 16S amplicon sequencing using the initial leaf compost (n = 3, air-dry conditions), bulk samples from all four treatments (n = 3, air-dry conditions), and MF from selected treatments (granite, coarse basalt, and fine basalt) (n = 1, wet conditions) after the incubation. The latter was a composite of three reps due to the limited mass recovery of MF. The DNA was extracted from 0.4 g of each sample by the FastDNA® SPIN Kit for Soil (MP Biomedicals, California, USA) according to the manufacturer's instructions with a few modifications. Quantitative PCR (qPCR) assays were conducted using the fluorescent dye SYBR Green (THUNDERBIRD Next SYBR qPCR mix, Toyobo) by a QuantStudio 3.0 real-time PCR System (Applied Biosystems/Thermo Fisher Scientific). 16S rRNA genes quantified using the primer pairs Bact1369F/ProK1492R (Suzuki et al., 2000) for the V3-V4 region of the 16S rRNA. The PCR reactions for 16S rRNA started with an initial denaturing step at 95 °C for 30 s, followed by 40 cycles at 95 °C for 5 s and 60 °C for 30 s. Melting curve analyses involved a denaturing step at 95 °C for 15 s, annealing at 65 °C for 1 min, and melting in 0.1 °C steps up to 95 °C. Standard curves for each assay were generated by serial dilutions of linearized plasmids with cloned fragments of environmental DNA. Amplification efficiencies were 96.4 %. 16S rRNA amplicon sequencing and subsequent bioinformatics analysis are the same as the previous studies (Bamba et al., 2024; Hara et al., 2024). DNA sequencing data (16S rRNA gene amplicon) are available at the NCBI Sequence Read Archive (SRA) under BioProject ID PRJDB18777. For the 16S rRNA amplicon, taxonomy was assigned to ASVs using the SINTAX algorithm (Edgar, 2016) implemented in USEARCH (v11.0.667) against the RDP database v18 (Cole et al., 2014).

2.7 Statistics and calculations

The effects of rock treatment on the measured variables were tested by one-way ANOVA, followed by a Tukey's post hoc test. The changes in variables before and after the incubation were evaluated using paired t-tests. All statistical analyses were performed in Microsoft Excel for Microsoft 365 MSO and Excel Toukei (BellCurve for Excel, Social Survey Research Information, Tokyo, Japan).

We estimated the total amounts of extractable metals in the rock-OM mixtures after the incubation by summing up the metals in LF, MF, and HF instead of the bulk sample values because we expected less sub-sampling error from the former. Specifically, roughly 44% of the mass of the incubated mixture was used for the density fractionation analysis, whereas only 13% was allocated for bulk sample chemistry. The high mass recovery of the density fractions (range: 99–101%, Table 1) suggests that this approach was appropriate.

Alpha and beta diversities of the bacterial communities in the initial leaf compost and post-incubation samples were calculated using the "phyloseq" pipeline (McMurdie and Holmes, 2013) and the "microeco" pipeline (Liu et al., 2021), respectively. Principal coordinate analysis (PCoA) of unweighted UniFrac distance was used to visualize beta diversity between the treatments. We estimated the influence of the mineral type in the rock-OM mixtures on the beta diversity by permutational multivariate analysis of variance (PERMANOVA) using the 'adonis' function in the 'vegan' package (Oksanen, 2013). We further analyzed the correlations between the bacterial composition and the property variables of MF and bulk samples on Day 55 and initial compost by the Mantel test using the 'mantel' function in the 'ecodist' package (Goslee and Urban, 2007). All the microbial analyses were performed using R version 4.2.0 (www.r-project.org).

We presented and discussed the mass, C and N, and extractable metal data of bulk and density fractions in multiple ways (e.g., per fraction vs. per bulk mass basis). Tables and figures of these data are summarized in Table S7.

3 Results

3.1 Recovery after density fractionation

Density fractionation of the rock-OM mixtures at the end of the 55-day incubation experiment showed reasonable recoveries for all the rock treatments: 99–101% for mass, 86–107% for C, 90–109% for N, 88–95% for extractable Al, 99–108% for extractable Fe, and 85–93% for extractable Si (Table 1). Metal recovery data is not available for granite and sand treatment as the metal extraction of LF and MF was not possible due to the limited mass. Some variations among the rock treatments were found. The coarse basalt treatment had less complete C and N recoveries than the other treatments and less complete extractable Al and Si recoveries relative to the fine basalt treatment. Overall, we considered that these recoveries were at acceptable levels for further assessment of the elemental distribution patterns across the density fractions.

Table 1. Recovery of mass, C, N, and extractable Al, Fe, and Si after the density fractionation of the rock-OM mixtures on Day 55.

	Mass (%)	C (%)	N (%)	Extractable Al (%)	Extractable Fe (%)	Extractable Si (%)
Granite 38–75 µm	100 ± <1	95 ± 12	100 ± 6	N.A.	N.A.	N.A.
Basalt 38–75 µm	99 ± 1	86 ± 8	90 ± 8	88 ± 7	99 ± 6	85 ± 3
Basalt 20–38 µm	100 ± <1	102 ± 1	106 ± 1	95 ± 3	108 ± 1	93 ± <1
Sand 100–300 µm	101 ± <1	107 ± 14	109 ± 18	N.A.	N.A.	N.A.

Al, Fe, and Si were extracted sequentially with sodium pyrophosphate, acid oxalate, and dithionite-citrate reagents.
Value shows mean ± standard deviation (n = 3).
N.A. Not analyzed due to the limited mass recovery of the meso-density fraction.

3.2 Mass, C and N, and $\delta^{13}C$ and $\delta^{15}N$

Mass proportion in MF after the incubation was the highest in the fine basalt (13%), followed by the coarse basalt (7.1%), granite (0.57%), and sand (0.17%) treatments (Fig. 2). The increases in MF largely corresponded to the reduction in the mass of HF. However, the initial granite, coarse basalt, and fine basalt contained small amounts of MF, accounting for 0.30%, 6.8%, and 6.3% of the initial mass of respective minerals (Fig. 3a). After accounting for the initial MF in these treatments, we detected a significant increase in the mass of MF after the incubation for the granite and fine basalt treatments (Fig. 3a). The largest increase in MF mass was found in the fine basalt treatment (65 mg g^{-1} bulk) whereas that in the coarse basalt and sand treatments changed little (0.26–3.0 mg g^{-1} bulk) over the 55-day duration.

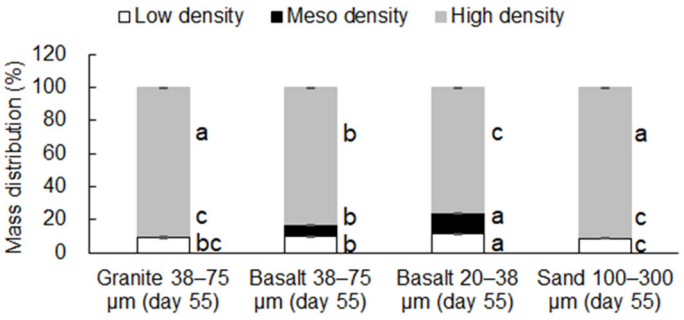

Figure 2. Mass distributions of the four rock-OM mixtures across low-, meso-, and high-density fractions on Day 55. For each density fraction (i.e., low-, meso-, or high-density), significant differences among the four rock treatments were shown by different letters at P < 0.05 (Tukey's test; n = 3).

The C concentration in LF on Day 0, the initial leaf compost, was 408 mg g^{-1} fraction (Table S8-1), whereas that on Day 55 ranged from 378 to 431 mg g^{-1} fraction (Table S9-1). The C distribution to LF differed among the treatments in the following order: fine basalt > coarse basalt > granite > sand (Table S9-2). The same pattern was found for MF and HF. Because the initial crushed rocks contained only small amounts of MF (Fig. 3a, Table S6) that had only trace level of C (Fig. 3b; Table S8-1, S8-2), the C increase in MF after the incubation was significant for all four treatments ($P < 0.01$, Fig. 3b). The largest increase was shown in fine basalt (1.50 ± 0.05 mg C g^{-1} bulk) followed by the coarse basalt (1.03 ± 0.07 mg C g^{-1} bulk) and then the granite (0.60 ± 0.06 mg C g^{-1} bulk) treatments. Even in the sand treatment, we detected a significant increase in the amount of C in MF (0.10 ± 0.01 mg C g^{-1} bulk). When summing up the C and N in all three fractions, the total amounts of C and N left after the incubation showed a significant difference among the treatments in the following order: fine basalt > coarse basalt > granite > sand (Table S9-2).

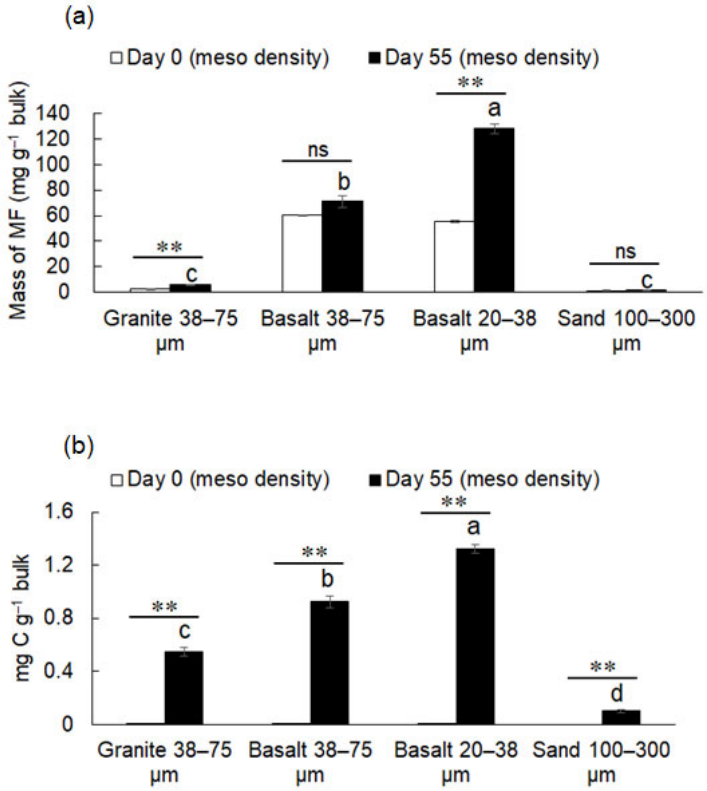

Figure 3. The mass of meso-density fraction (MF) in the rock-OM mixtures before (Day 0) and after the incubation (Day 55) (a). The amounts of C in MF in the bulk mixtures on Day 0 and Day 55 (b). Significant differences among the rock treatments on Day 55 are shown by different letters at $P < 0.05$ (Tukey's test; $n = 3$). The increase in MF from Day 0 to Day 55 is shown with asterisks (** significance at $P < 0.01$; ns, not significant).

The C:N ratio of the initial leaf compost and that of LF after the incubation were similar in all four treatments (Fig. 4a, Table S9-1) because the majority of C was present in LF. Among the density fractions, the C:N ratio progressively declined with increasing density. In other words, more C was lost relative to N from LF towards HF during the incubation. The isotopic values ($\delta^{13}C$ and $\delta^{15}N$) of initial leaf compost and those of LF after the incubation were similar in both basalt treatments (Fig. 4b, 4c). The value of $\delta^{13}C$ significantly increased from LF towards HF, whereas $\delta^{15}N$ showed a significant increase from LF to MF and a slight decline from MF to HF (Fig. 4b, 4c).

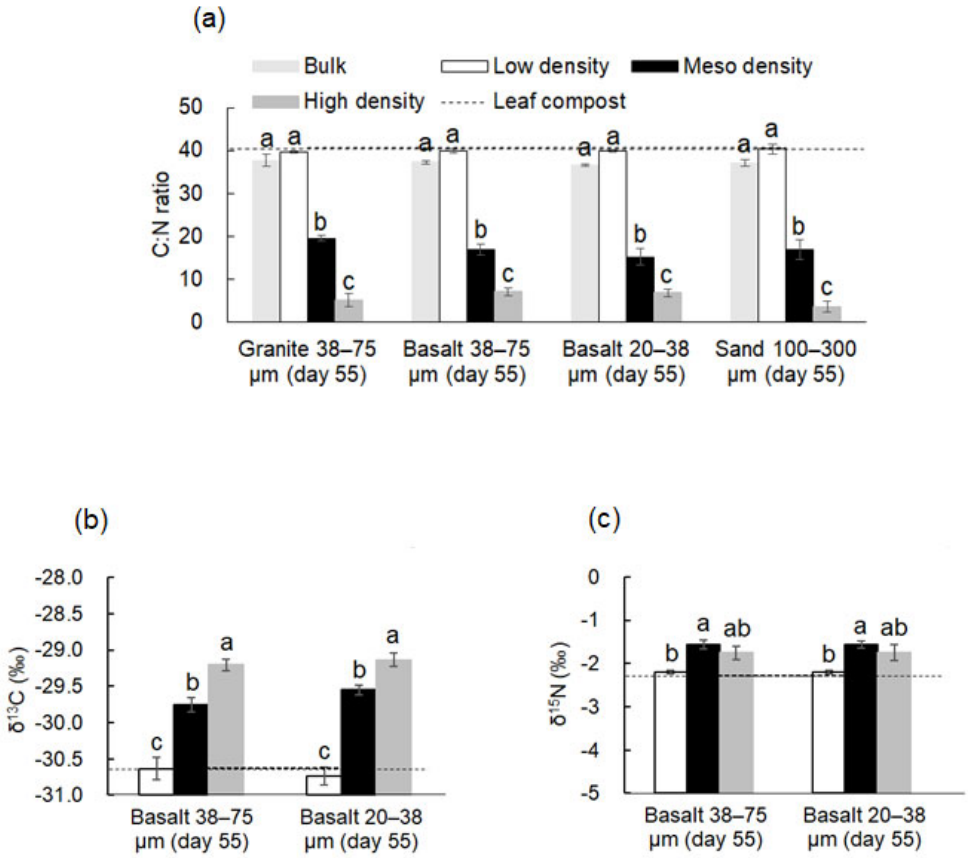

Figure 4. C:N ratio (a), $\delta^{13}C$ (b), and $\delta^{15}N$ (c) among the density fractions from the four rock treatments on Day 55 and those of initial leaf compost as a horizontal dotted line. No $\delta^{13}C$ and $\delta^{15}N$ analyses were done for granite and sand treatment due to the limited mass of MF. Significant differences among the density fractions are shown with different letters at $P < 0.05$ (Tukey's test; $n = 3$).

3.3 Extractable Al, Fe, and Si and pH

Initial sand contained only negligible amounts of OX-extractable metals ($metal_{OX}$), and initial granite contained < 1 mg g^{-1} bulk of $metal_{OX}$, whereas initial coarse and fine basalts contained much greater extractable metals (Table S2). Between the two basalt size treatments, fine basalt had a higher amount of PP-extractable Al, Fe, and Si (Al_{PP}, Fe_{PP}, Si_{PP}) as well as Al_{OX}, Fe_{OX}, and Si_{OX} compared to coarse basalt.

After the 55-day incubation, the metal concentrations in LF consistently increased for Fe_{OX}, Fe_{DC}, Fe_{PP}, and Al_{PP} among the four rock treatments, but especially for the basalt treatments (Table 2; Table S10-1). For the basalt treatments where enough MF mass recovery allowed the metal extractions (Fig. 2), a major increase in metal concentration was shown in Fe_{OX}, Al_{OX}, Si_{DC}, and Al_{PP} for fine basalt, and Si_{DC} and Al_{PP} for coarse basalt. In HF, major changes were the decline in Fe_{OX} and Al_{OX} concentration for coarse basalt (Table 2; Table S10-1).

Table 2. Concentrations (mg g^{-1} per fraction) of Al, Fe, and Si dissolved by sequential extractions in each density fraction from the rock-OM mixtures on Day 55.

	Sodium pyrophosphate (PP)						Acid oxalate (OX)						Dithionite-citrate (DC)						Total					
	Al		Fe		Si		Al		Fe		Si		Al		Fe		Si		Al		Fe		Si	
Low-density fraction (< 1.8 g cm^{-3})																								
Granite 38–75 µm	0.33	± 0.03	0.25	± <0.01	3.0	± 0.1	1.0	± <0.1	1.7	± <0.1	0.51	± 0.01	0.30	± 0.03	1.5	± 0.1	2.7	± 0.2	1.6	± 0.1	3.4	± 0.1	6.2	± 0.3
Basalt 38–75 µm	0.48	± 0.01	0.53	± 0.02	2.0	± 0.1	1.4	± 0.1	3.3	± 0.1	0.67	± 0.02	0.37	± 0.01	2.1	± <0.1	4.0	± 0.1	2.2	± 0.1	5.9	± 0.1	6.6	± 0.1

Basalt 20–38 µm	0.52	± 0.02	0.71	± 0.02	1.6	± <0.1	2.0	± 0.1	6.3	± 0.1	1.2	± <0.1	0.48	± 0.01	3.3	± 0.1	6.4	± 0.1	3.0	± <0.1	10	± <1	9.2	± 0.1
Sand 100–300 µm	0.39	± 0.01	0.24	± <0.01	3.1	± 0.2	1.1	± 0.1	1.6	± <0.1	0.49	± 0.03	0.26	± 0.04	1.1	± 0.1	2.4	± 0.3	1.7	± 0.1	3.0	± 0.1	6.0	± 0.4
Meso-density fraction (1.8–2.4 g cm^{-3})																								
Granite 38–75 µm	N.A.		N.A.		N.A.		N.A.		N.A.		N.A.		N.A.		N.A.		N.A.		N.A.		N.A.		N.A.	
Basalt 38–75 µm	0.44	± 0.01	0.76	± 0.04	1.7	± <0.1	13	± 3	51	± 11	6.1	± 1.3	2.7	± 0.1	16	± 1	9.6	± 0.2	17	± 3	68	± 11	17	± 1
Basalt 20–38 µm	0.44	± <0.01	0.69	± 0.02	1.7	± <0.1	18	± 1	74	± 1	9.4	± 0.2	2.4	± 0.1	14	± <1	9.2	± 0.1	21	± 1	89	± 1	20	± <1
Sand 100–300 µm	N.A.		N.A.		N.A.		N.A.		N.A.		N.A.		N.A.		N.A.		N.A.		N.A.		N.A.		N.A.	
High-density fraction (> 2.4 g cm^{-3})																								
Granite 38–75 µm	0.0	± <0.1	0.0	± <0.1	0.0	± <0.1	0.12	± 0.02	0.68	± 0.04	0.13	± 0.02	0.18	± 0.01	1.8	± 0.0	0.73	± 0.02	0.30	± 0.03	2.5	± 0.1	0.86	± 0.04
Basalt 38–75 µm	0.071	± 0.011	0.23	± 0.01	0.36	± 0.02	3.7	± 0.1	25	± 1	2.2	± 0.1	0.72	± 0.04	4.8	± 0.3	8.9	± 0.2	4.5	± 0.1	30	± 1	11	± <1
Basalt 20–38 µm	0.15	± <0.01	0.28	± <0.01	0.57	± 0.02	4.7	± 0.1	34	± 1	3.1	± <0.1	0.59	± 0.05	4.9	± 0.6	9.2	± 0.1	5.4	± 0.1	39	± 1	13	± <1
Sand 100–300 µm	0.0	± <0.1	0.0	± <0.1	0.0	± <0.1	0.015	± 0.008	0.14	± 0.10	0.0	± <0.1	0.087	± 0.014	1.3	± 0.3	0.080	± 0.021	0.10	± 0.01	1.4	± 0.4	0.080	± 0.021

Al, Fe, and Si were extracted sequentially with sodium pyrophosphate, acid oxalate, and dithionite-citrate reagents.
Value shows mean ± standard deviation (n = 3).
N.A. Not analyzed due to the limited mass recovery of the meso-density fraction.
Concentrations (per fraction) on Day 0 are represented in Table S10-1.

The distribution of these metal phases across the density fractions, accounting for their masses, showed that the initial rock-OM mixtures held most of the extractable metal phases in HF (Table S10-2) and that the incubation led to enrichment of Fe, Al, Si, especially oxalate-extractable phases, in MF for the two basalt treatments (Table S11). Overall, the distribution of total extractable Fe in MF changed from 11-12% to 16-27% of the respective bulk samples (i.e., LF+MF+HF at Day 0 and 55) (Table S10-2, S11). Similarly, total extractable Al also increased from 15-19% to 23-38% and Si showed a similar pattern. Among the three extractactions, major increases over the incubation occurred in Fe_{OX}, Al_{OX}, and Si_{OX} phases in MF particularly for fine basalt treatment, which was in part balanced by their decreases in HF (Table S10-2, S11). Similar but weaker trends were shown for Fe_{DC}, Al_{DC}, and Si_{DC} phases, while the changes in pyrophosphate-extractable phases remain minor. On a bulk sample basis, total extractable Fe in MF increased from 3.6–4.2 to 4.9–11 mg g^{-1} and Al from 0.88–1.0 to 1.2–2.7 mg g^{-1} during the incubation. Concurrently, the total extractable Fe in HF slightly decreased from 28–30 to 25–29 mg g^{-1} and Al from 4.2–4.9 to 3.7–4.1 mg g^{-1} during the incubation. These changes mainly occurred in oxalate-extractable phases: Al_{OX} and Fe_{OX} in MF after the incubation accounted for 82–89% and 76–86% of the total extractable metal pools, respectively (Table S11). As a result, MF showed statistically detectable increases (thus accumulation) of Al, Fe, and Si, especially in OX-extractable pools, for fine basalt (Fig. 5a-c), whereas a small but significant increase in Al_{PP} phase was shown for coarse basalt. Meso-density fraction also showed significant enrichment of Fe_{OX} for both basalt treatments and that of Al_{OX} for the coarse basalt treatment relative to Si_{OX} (Table 3). In addition, Fe_{OX} phase appeared to be enriched relative to Al_{OX} phase in fine basalt treatment. The carbon-to-extractable metal molar ratios ranged from 0.5 to 2.3 (Table S12).

When summing up the total extractable Al and Fe among the three fractions, a significant increase after the incubation period was detected for Fe (7.2 mg g^{-1} bulk) and Al (1.7 mg g^{-1} bulk) only in fine basalt treatment (Table S10-2, S11). Thus, the observed changes in the extractable metals among the fractions likely resulted from both basalt weathering and redistribution in fine basalt and only from the redistribution in the other treatments.

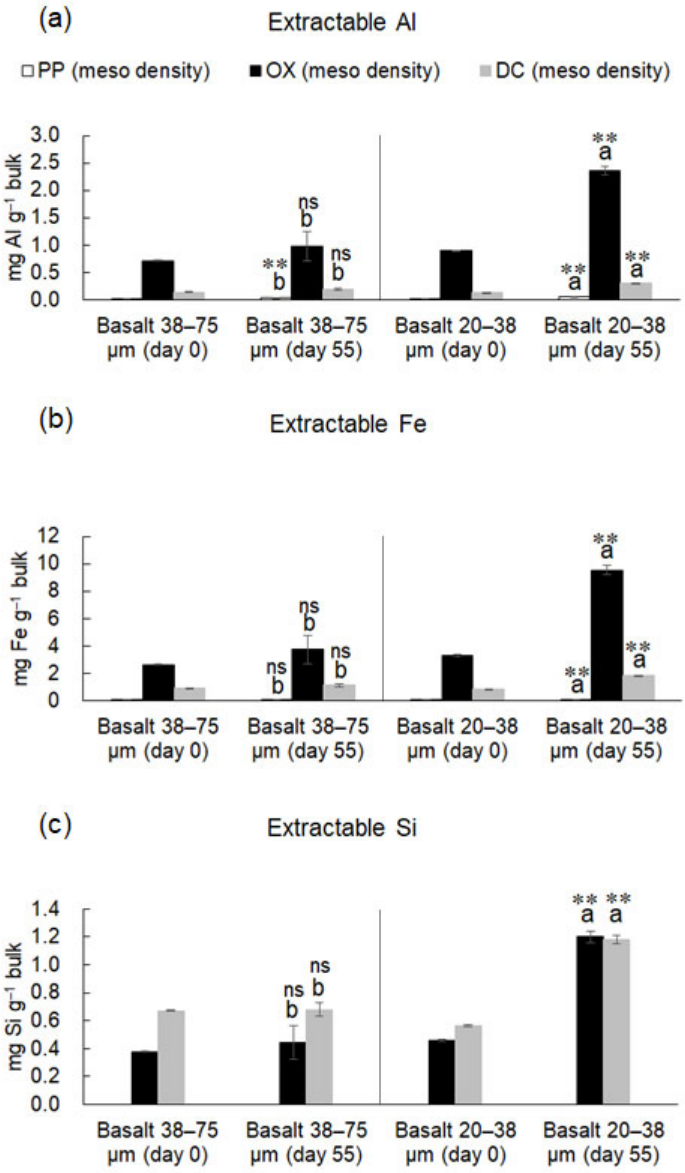

Figure 5. Amounts of extractable Al (a), Fe (b), and Si (c) in MF from the rock-OM mixtures on Day 0 and Day 55. See Figure 3 legend for statistical difference signs.

375 The pH(H_2O) of the bulk samples of all treatments on Day 55 ranged between 6.5 and 7.6, with the highest pH in the fine basalt treatment, followed by the coarse basalt, while the granite and sand treatments were slightly acidic (Table 4). The difference in pH(KCl) among the treatments was less clear.

Table 3. Molar ratios of acid oxalate extractable Al, Fe, and Si in meso-density fraction in the two basalt treatments before and after the
380 55-day incubation.

		Meso-density fraction (1.8–2.4 g cm^{-3})								
		Al:Si			Fe:Si			Fe:Al		
Basalt 38–75 µm	Day 0	2.0	± <0.1		3.5	± <0.1		1.8	± <0.1	
	Day 55	2.3	± <0.1	**	4.2	± 0.1	**	1.8	± <0.1	ns
Basalt 20–38 µm	Day 0	2.0	± <0.1		3.6	± <0.1		1.8	± <0.1	
	Day 55	2.0	± <0.1	ns	4.0	± <0.1	**	2.0	± <0.1	**

Value shows mean ± standard deviation (n = 3).

The increase in molar ratio from Day 0 to Day 55 is shown with asterisks (** significance at $P < 0.01$; ns, not significant, *t*-test).

Table 4. pH of the rock-OM mixtures after the 55-day incubation.

	pH(H_2O)			pH(KCl)		
Granite 38–75 µm	6.7	± <0.1	c	6.1	± <0.1	a
Basalt 38–75 µm	7.3	± <0.1	b	5.9	± <0.1	bc
Basalt 20–38 µm	7.6	± <0.1	a	6.0	± <0.1	ab
Sand 100–300 µm	6.5	± <0.1	d	5.8	± <0.1	c

Value shows mean ± standard deviation ($n = 3$).

Significant differences among the rock treatments on Day 55 are shown by different letters at $P < 0.05$ (Tukey's test; $n = 3$).

3.4 Leaching loss of elements and leachate chemistry

The total amount of DOC released from the rock-OM mixtures during the eight repeated leaching events was 13–15 mg C per incubation column (Table 5), which was equivalent to 1.3–1.5% of the total C in the initial mixtures. No significant difference in DOC release was found among the four treatments. For the major rock-forming elements, Fe leaching was the highest in the fine basalt, followed by the coarse basalt treatment, and Si leaching showed similar patterns (Table 5). Conversely, the total amount of Al leached was the highest in the sand and the lowest in the coarse basalt treatment. The sum of base cations leached was the highest in the fine basalt treatment, followed by the coarse basalt, sand, and granite treatments. Leaching of base cations during the incubation followed the order: Ca > Na > K > Mg. Greater leaching of Na from fine basalt relative to coarse basalt was consistent with (Yang et al., 2026), which likely indicates rapid dissolution of Na plagioclase from the basaltic rock. The pH of the leachates was neutral to alkaline (7.1–9.1), with the highest pH in the fine basalt, followed by the coarse basalt treatment, while the other two treatments had nearly neutral pH (Table 4). The observed pH difference largely corresponded to the variation of the leachate chemistry among the treatments (e.g., Na, Ca, and Al).

Table 5. Amounts of DOC, Al, Fe, Si, base cations, and pH in leachates released from the rock-OM mixtures during the 55-day incubation (the sum of the eight repeated leaching events).

	DOC (mg)			Al (mg)			Fe (mg)			Si (mg)		
Granite 38–75 µm	14	± 1	a	0.0068	± 0.0019	ab	0.015	± 0.001	c	1.5	± 0.1	b
Basalt 38–75 µm	13	± <1	a	0.0044	± 0.0007	b	0.028	± 0.001	b	3.5	± <0.1	a
Basalt 20–38 µm	15	± <1	a	0.0060	± 0.0009	ab	0.036	± <0.001	a	4.5	± 0.2	a
Sand 100–300 µm	13	± 1	a	0.010	± 0.001	a	0.013	± <0.001	c	1.7	± 0.4	b

	Sum of base cations (mg)			Na (mg)		Ca (mg)		K (mg)		Mg (mg)		pH		
Granite 38–75 µm	7.7	± 0.3	c	1.6	± <0.1	4.2	± 0.2	0.94	± 0.06	1.0	± 0.1	7.2	± <0.1	c
Basalt 38–75 µm	9.8	± 0.3	b	2.0	± 0.1	5.5	± 0.2	1.7	± <0.1	0.62	± 0.04	7.9	± 0.1	b
Basalt 20–38 µm	14	± <1	a	6.1	± 0.2	5.4	± 0.1	1.6	± <0.1	0.49	± 0.02	9.1	± <0.1	a
Sand 100–300 µm	8.9	± 0.7	bc	1.2	± 0.2	3.3	± 0.4	3.3	± 0.3	1.1	± 0.1	7.1	± 0.1	c

Value shows mean ± standard deviation ($n = 3$).

Significant differences among the rock treatments on Day 55 are shown by different letters at $P < 0.05$ (Tukey's test; $n = 3$).

3.5 Microscopic observations of organo-mineral assemblage by SEM and STXM-NEXAFS

We observed some shaking-resistant, organo-mineral assemblages in the post-incubation MF (Fig. 6). The observed assemblages were present as microaggregates of 100–200 mm in diameter, consisting of crushed rocks (Fig. 6b, 6d, 6f) and OM, including fungal hyphae (Fig. 6d). Greater aggregate sizes were apparent in the two basalt treatments compared to the granite treatment (Fig. 6d, 6f). Much finer subunits (rock fragments) were confirmed in the fine basalt aggregates compared to the coarse basalt aggregates.

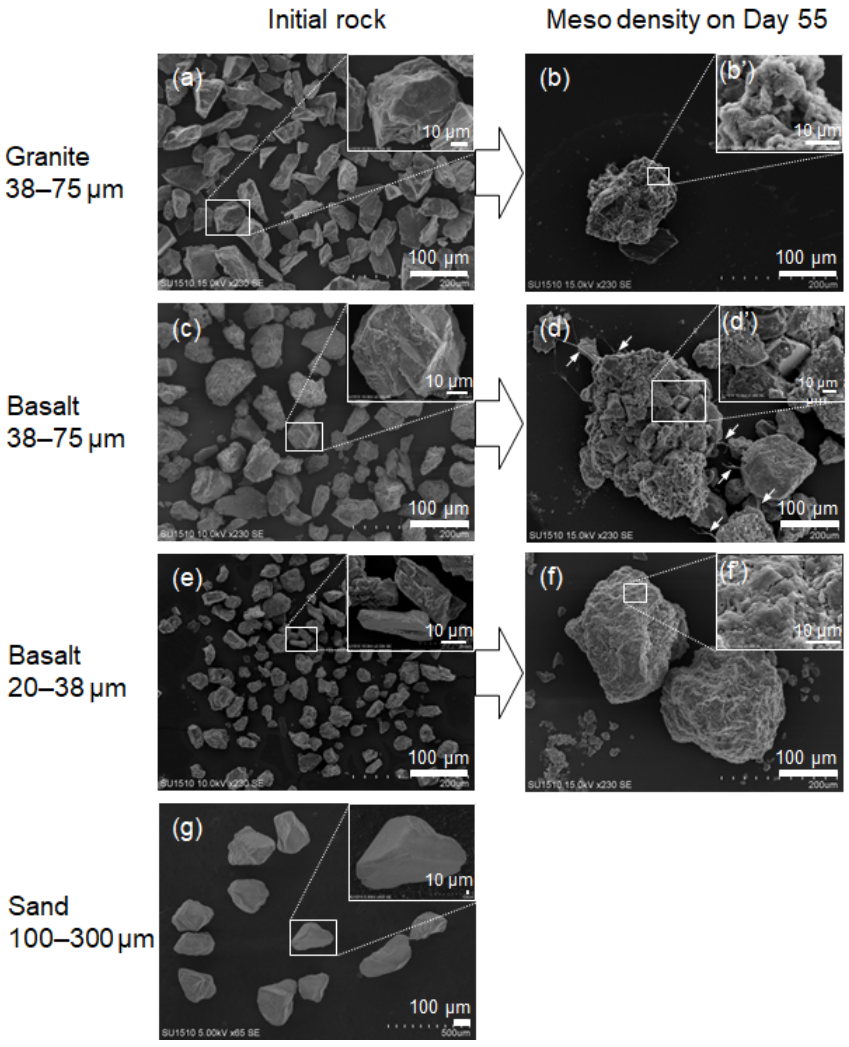

Figure 6. SEM images of the crushed rock minerals and the isolated density fraction. (a) initial granite, (b) MF of granite, (c) initial coarse basalt, (d) MF of coarse basalt, (e) initial fine basalt, (f) MF of fine basalt, and (g) initial sand. Fungal hyphae were shown with arrows (d).

The subsamples of dispersed MF material from the selected rock-OM mixtures, the granite and coarse basalt treatments (see Fig. S4 for SEM images), were further characterized to assess the chemical nature of the organo-mineral assemblages by STXM-NEXAFS (Fig. 7). We first obtained the spatial distribution of C, Al, and Fe for a large area (35 × 35 µm, Fig. 7A, 7B). As the C-rich zones in the targeted assemblage were patchy, we selected one of these patches and the adjacent mineral-rich zones as a focused area (5 × 5 µm) to examine the distribution of C functional groups (Fig. 7a, 7b). In the granite sample, the C-rich zone (shown as ROI in Fig. 7a) was relatively enriched in aromatic and carboxylic C compared to the average C K-edge NEXAFS spectra of the entire 5 × 5 µm area (Fig. 7a1, 7a3). While some overlaps of C with Fe and Al (Fig. 7a4, 7a5) were shown, the metal-rich patches appeared to be present adjacent to, rather than overlapped with, the C-rich zone. The dominance of Fe over Al shown in the coarse basalt treatment (Fig. 7B) was in line with the higher content

and increase of Fe_{OX} relative to Al_{OX} phase (Fig. 5a, 5b). In the coarse basalt sample, the C-rich zone (ROI in Fig. 7b) was enriched in ketonic C in contrast with the granite sample (Fig. 7b2). Aromatic C and carboxylic C appeared to be distributed separately (Fig. 7b1, 7b3). While the three major C peaks were found in MF from both granite and coarse basalt, the latter appeared to have a higher relative abundance of ketonic C (Fig. 7, middle left spectra).

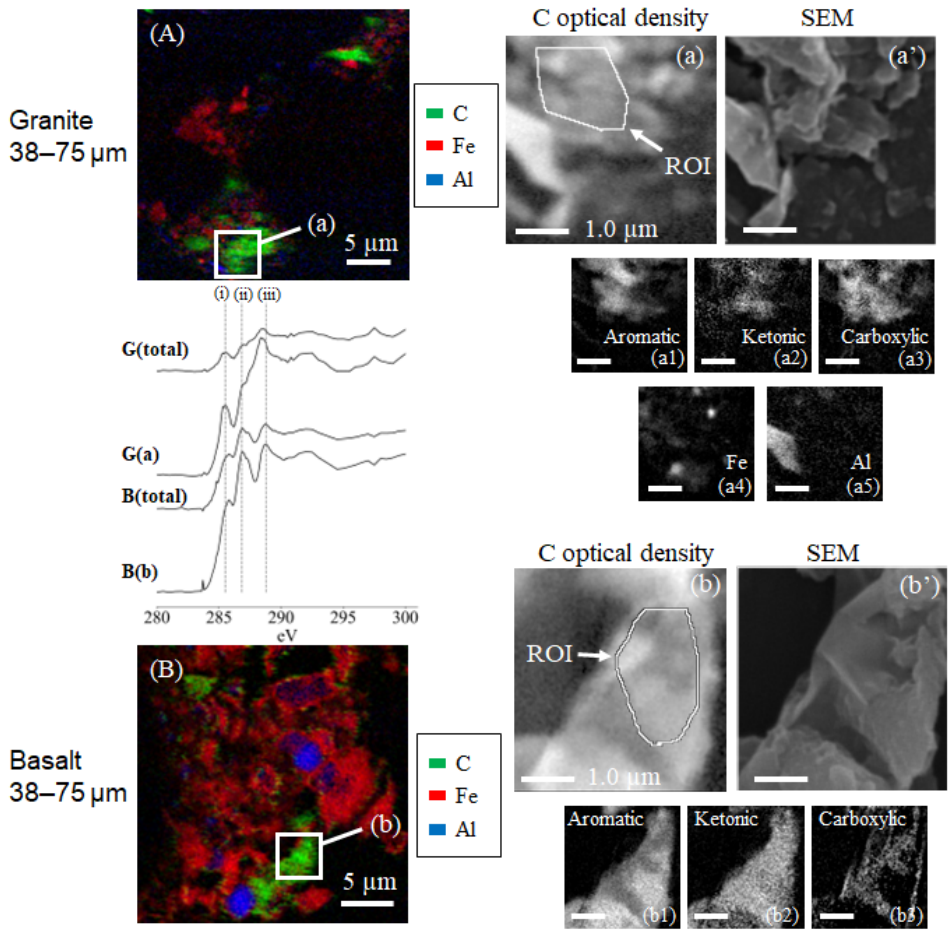

Figure 7. The elemental maps obtained with STXM-NEXAFS analysis. The images show the distribution of elements in the 35 x 35 µm region of interest for MF of granite (A) and 30 x 30 µm region of interest for coarse basalt treatments (B) after the 55-day incubation, respectively. C optical density (a, b) and SEM (a', b') images for a selected C-rich region at higher resolution (5 x 5 µm and 4 x 4 µm, respectively). The C K-edge NEXAFS spectra in the middle left panel show the image stacks for the 35 x 35 µm region of granite, G(total), and coarse basalt, B(total), and for the C-rich regions of granite, G(a), and coarse basalt, B(b). Dashed lines (i), (ii), and (iii) represent the energy levels at 285.5, 286.8, and 288.8 eV corresponding to aromatic C, ketonic C, and carboxylic C. The images (a1), (a2), and (a3) and (b1), (b2), and (b3) show the spatial distribution of specific C type, aromatic C, ketonic C, and carboxyl C, respectively, in the higher resolution images. The distribution of Fe (a4) and Al (a5) was measured only for the granite sample due to beamtime limitations.

3.6 Bacterial community composition after the 55-day incubation

We assessed the effect of the rock treatment on the microbial community composition at the end of the incubation using bacterial amplicon sequencing. The bacterial copy number ranged from 3.7 x 10^8 to 1.5 x 10^9, and the initial compost tended to have a higher number than the bulk samples after the incubation (Table S13). Among the post-incubation bulk samples, the bacterial number decreased in the following order: sand > granite > two basalt treatments, with no significant difference among the treatments (ANOVA, $P = 0.08$). The alpha diversity indices, including Chao1, Shannon index, and evenness, showed no significant differences among the treatments (Table S13; ANOVA, $P = 0.28$, 0.24, 0.10, respectively). Notably, the beta diversity (PCoA plot; Fig. 8a) was different among the treatments (PERMANOVA, $F = 5.63$, $P = 0.001$), while the top three phyla —Proteobacteria, Actinobacteria, and Firmicutes—were commonly observed across the samples (Fig.8b).

The sum of the relative abundance of the three ASVs belonging to Neobacillus (Fig.8c), the most dominant genus, was higher in MF compared to the bulk sample (15.5 ±8.4 % and 3.5 ±1.7 %, respectively, *t*-test, $P = 0.0036$). The mantel results using the data of MF and the bulk samples on Day 55 further showed significant correlations between the microbial composition (PCoA score) and selected soil properties including total C, total N, pH(KCl), pH(H_2O), Fe_{PP}, and Al_{PP} (R^2 = 0.86, 0.86, 0.82, 0.80, 0.30 and 0.22 respectively, $P < 0.05$; Table S14).

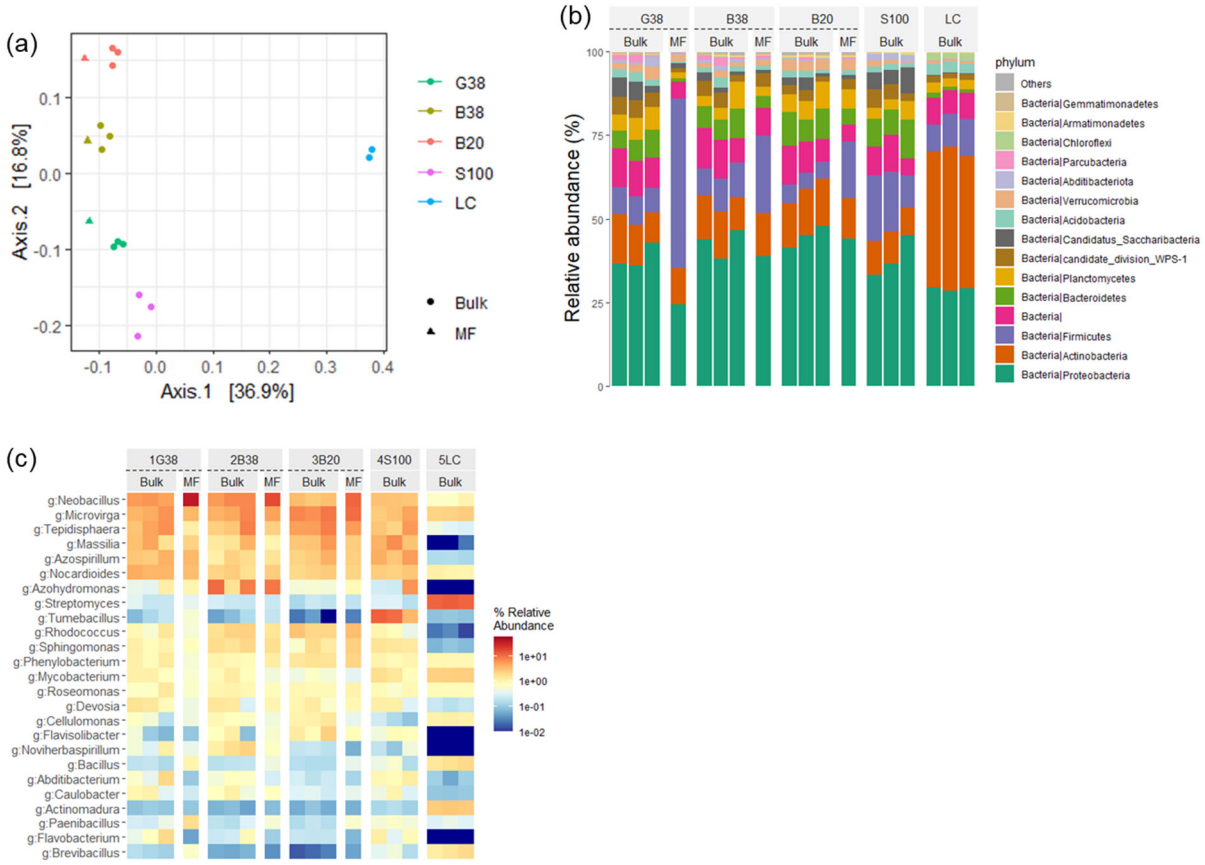

Figure 8. Beta diversity shown by PCoA plot based on 16S rRNA gene (a), bar plot at phylum level (b), and heatmap at genus level (c) in bulk and MF samples. G38: granite 38–75 µm (Day 55), B38: basalt 38–75 µm (Day 55), B20: basalt 20–38 µm (Day 55), S100: sand 100–300 µm (Day 55), and LC: initial leaf compost.

4 Discussion

4.1 Formation of organo-mineral assemblages via weathering-derived metal supply

We conducted a simple incubation experiment to test whether Fe and Al released from rock weathering promote the formation of organo-mineral assemblage, represented by the meso-density fraction (MF), and to assess the concurrent changes in both organic matter (OM) and rock-derived elements. Among the three crushed rocks used, fine basalt showed the highest increases in MF mass (Fig. 3a), C content (Fig. 3b), and extractable metals and metalloid particularly Fe_{OX}, Al_{OX}, and Si_{OX} (Fig. 5). Over the 55-day incubation period, C accumulation in MF was measured at 1.3 ± 0.1 mg C g^{-1} bulk for fine basalt, 0.9 ± 0.1 mg C g^{-1} bulk for coarse basalt, and 0.6 ± 0.1 mg C g^{-1} bulk for granite (Table S8-2, S9-2). Extractable Fe, Al, and Si in MF also showed the same trend for the basalt treatments (Table S10-2, S11). The concurrent enrichment of mineral-associated OM (MAOM) and extractable metals supports the idea that metal release from basalt weathering directly facilitates the formation of organo-mineral assemblages, consistent with the *organo-metallic glue* hypothesis (Wagai et al., 2020).

The hypothesis proposes that the assemblage (aggregation) occurs through organo-metallic binding agents that can form

through organo-metal complexation and coprecipitation as well as dissolved OM sorption on secondary metal oxide phases. Identifying the sources for the metal enrichment in MF provides insight into the formation mechanism. Mass balance of the extractable metals before and after the incubation is, however, quite challenging due to relatively high errors in metal extractions, especially when having multiple extractions and fractions. While our results are subject to these errors, we postulated potential dynamics of Fe and Al phases for the fine basalt treatment where the largest changes were detected. On bulk sample basis, net increases in total extractable Fe was found in MF (7.3 ± 0.7 mg Fe g^{-1}) and LF (0.9 ± 0.04 mg Fe g^{-1}) while net decrease in HF (-0.9 ± 1.1 mg Fe g^{-1}) during the incubation period (Fig. 9). Then, the net increase of 7.2 ± 1.8 mg Fe g^{-1} (i.e., LF + MF + HF) likely resulted from the basaltic rock weathering. Unfortunately, we did not detect the net Fe increase when comparing the bulk samples before and after the incubation (data not shown) due presumably to errors associated with colloidal Fe (e.g., for colloidal Fe even after high-speed centrifugation, Wagai et al., 2018). On the other hand, mass baslance was more reasonable for the total extractable Al: the increase in MF (1.7 ± 0.1 mg Al g^{-1}) and LF (0.1 ± 0.01 mg Al g^{-1}) and concurrent decrease in HF (0.1 ± 0.1 mg Al g^{-1}) resulted in the net increase in 1.7 ± 0.2 mg Al g^{-1} (Fig. 9), which was relatively close to the net increase detected in bulk sample (+0.4 ± 0.2 mg Al g^{-1}). These results, thus, suggest that nearly all Fe and Al released from basaltic rock may be preferentially retained in MF, even though approximately 80% of the basalt particles themselves were present in HF (Table S6). In other words, the majority of weathering-derived Fe and Al appeared to be present as precipitates of organo-metallic phase rather than secondary mineral phases (e.g., ferrihydrite). If the metals had precipitated primarily as secondary minerals, they should have been more concentrated in HF as coatings on basalt particle surfaces. Instead, their enrichment in MF (and, to some extent, in LF) found here implied preferential metal association with OM.

We, therefore, infer that the metals (and metalloids) released from basaltic rock rapidly complexed with, or coprecipitated with, dissolved OM and fine-sized particulate OM (POM) derived from leaf compost, prior to the formation of secondary metal oxide. The metal- and OM-rich phases likely enhanced particle cohesion by linking less reactive constituents (basalt grains and residual POM), thereby promoting the formation of physically stable organo-mineral assemblages represented by MF. The inferred sequence – metal release → preferential association with OM → aggregation – provides direct experimental support for the *organo-metallic glue* hypothesis, as depicted in (Fig. 10).

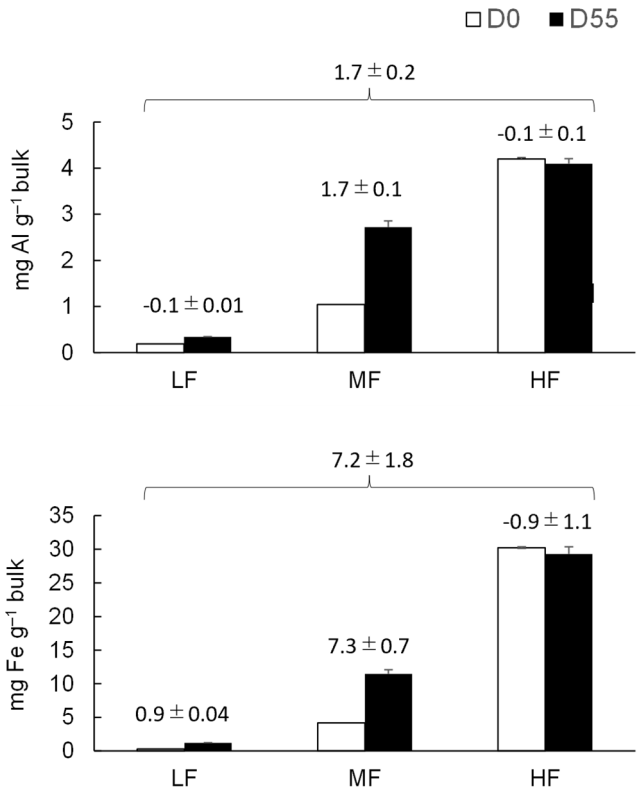

Figure 9. The changes in total extractable Al (a) and Fe (b) before and after the 55-day incubation in LF, MF, and HF on a bulk sample mass basis. Values ± SD above the two columns represent the change from Day 0 to Day 55. The sum of the changes across LF, MF, and HF was shown on the top of the three fractions.

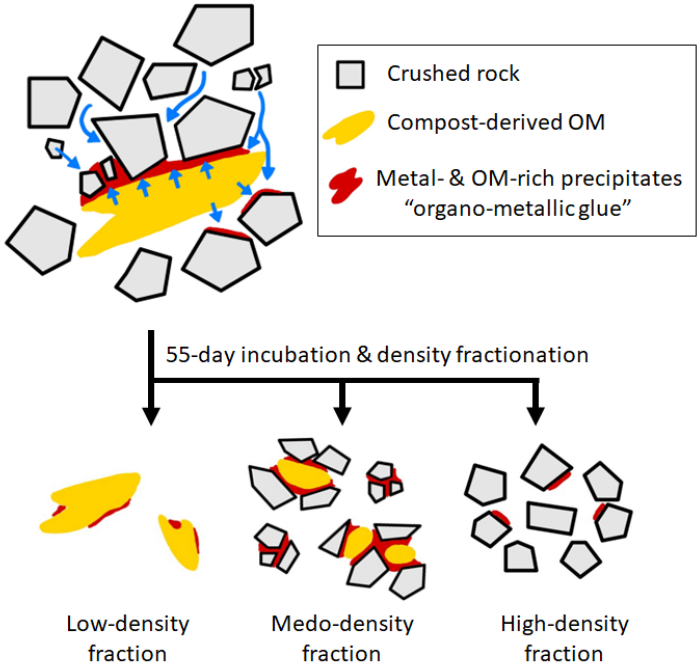

Figure 10. Conceptual synthesis of the experimental results in the context of the organo-metallic glue hypothesis. Metals (primarily Fe and Al) released from crushed rock under wet conditions were preferentially associated with dissolved and particulate OM, forming organo-metallic precipitates on mineral and organic particle surfaces upon drying. Following eight wet-dry cycles with physical mixing, these precipitates became enriched in the meso-density fraction, supporting their role as "glue" to bind mineral and organic particles to form physically stable organo-mineral aggregates.

4.2. Chemistry of the organo-mineral assemblages

Chemical characterization of MF provides further insights into the nature of the presumed *organo-metallic glue*. The dominance of Fe_{OX} and Al_{OX} relative to Fe_{PP} and Al_{PP} phases in the basalt treatments (Table S11) indicates that readily soluble organo-metal complexes were minor. The accreted OM in MF was thus more likely to be associated with Fe_{OX} and Al_{OX} phases through adsorptive or coprecipitation mechanisms. Microscopic observation of a representative MF microaggregate in the coarse basalt treatment (Fig. 7B) showed Fe dominance with patchy distributions of Al and C (rich in ketonic C). This pattern implies that Fe_{Ox} phases (as inferred from Fig. 5b) might have entrapped small OM-rich domains during coprecipitation. Given that only a limited area was analyzed, broader generalization across all MF materials is not warranted.

The C: (Fe+Al) molar ratio of newly-formed MF is consistent with the coprecipitate interpretation. For the fine basalt treatment, the ratio of 0.58 ± 0.03 (mol:mol), after accounting for the total extractable metals originally present in the basalt, falls within the range reported for laboratory-synthesized Fe-OM, Al-OM, and Fe-Al-Si-OM coprecipitates (Kleber et al., 2015; Tamrat et al., 2019; Jamoteau et al., 2023). This ratio was substantially lower than those for MF in natural soils (Wagai et al., 2020) and for organo-metal complexes typical of Andisols and spodic horizons (Takahashi and Dahlgren, 2016; Lundström et al., 2000), suggesting that the MF formed in our experiment contained relatively metal-rich, OM-poor precipitates. The relatively low C:metal ratios coincide with enrichment of Fe_{OX} and, to some extent, and Al_{OX} relative to Si_{OX} (Table 3), implying a greater role of Fe_{OX} phase for the organo-mineral assemblage formation. Assuming that the weathering-derived Fe_{OX} phase (Fig. 5b) consists entirely of ferrihydrite, the accreted OM in MF corresponds to 108 ± 6 mg C g^{-1} oxide – a value comparable to the maximum sorptive capacity of ferrihydrite for dissolved OM under laboratory conditions (Tipping, 1981; Kaiser et al., 1997). This result suggests that the surface of Fe_{OX} mineral phase was nearly

saturated by OM.

The metal- and OM-rich phases observed in MF may reflect either coprecipitation of metals with organic ligands or the spatial co-occurrence of metal oxides and OM (e.g., OM sorption on oxides or metal precipitation on organic surfaces). Because these two mechanisms cannot be distinguished with the available data, we collectively refer to the resulting phases as organo-metallic precipitates (Fig. 10).

We made a first-order approximation of the organo-metallic precipitates, recognizing that the calculation relies on simplified assumptions that Fe and Al occurred as ferrihydrite and allophane and OM consisted of 50% C. This component accounted for approximately a quarter of the total MF mass, suggesting that resultant Fe-Al-OM precipitates may be abundant enough to bind the remaining solids (mainly basalt particles with minor POM) into stable organo-mineral assemblages (Fig. 10). In addition, other major elements released from rocks (particularly Si and Ca) may synergistically contribute to the assemblage formation (Oades, 1988; Jamoteou et al., 2025).

4.3. Organic matter dynamics during assemblage formation

Several lines of evidence point to preferential accretion of microbially-processed, N-rich OM during organo-mineral assemblage formation. First, the C:N ratio of OM in MF sample was significantly lower than that in LF in all four rock-OM mixtures on Day 55 (Fig. 4a), suggesting a greater contribution of microbially altered material in MF. Second, MF had higher $\delta^{13}C$ and $\delta^{15}N$ values (+0.88–1.2‰ and +0.63–0.64‰, respectively) relative to LF in basalt treatments (Fig. 4b, 4c). The negative $\delta^{15}N$ values observed are within the common range for temperate forest leaves (−2.8 ± 2.0‰; Martinelli et al., 1999) and for organic layers of forest soils in the temperate climate zone (–0.3 ± 0.3‰; Choi et al., 2020), which likely reflects tree-leaf origin of the OM used in our study. Leaf compost itself contains a variety of plant- and microbially-derived compounds. Thus, the observed isotopic enrichment in MF cannot be fully attributed to microbial reactions that took place during the incubation. Our results are, nonetheless, consistent with previous field studies showing the increase in $\delta^{13}C$ and $\delta^{15}N$ with soil particle density (Sollins et al., 2009; Hatton et al., 2012; Moni et al., 2012). Importantly, HF contained small amounts of even stronger stoichiometric (Table S9-1, Fig. 4a) and isotopic (Fig. 4b) signatures than MF. These results suggest that some of decomposing POM fragments were likely occluded in MF, while HF primarily retained adsorbed microbial OM. The role of POM in MF formation aligns with its well-known role as hotspots for microbial activity and dissolved OM production, which may induce localized dissolution of minerals (e.g., Bölscher et al. 2025).

These findings are in line with the conceptual framework previously proposed (Fig. 7b in Wagai et al., 2020). STXM-NEXAFS spectra (Fig. 7) further suggest that C spectra of MF resemble those of typical soil OM (Solomon et al., 2012; Chen et al., 2014; Prietzel et al., 2018), which is dominated by microbially-processed OM in mineral soils (Sollins et al., 2009; Heckman et al., 2022). Our incubation conditions (wet-dry cycles, high temperature, and inoculation at each cycle) likely promoted microbial turnover and supply of microbial residues such as cell wall fragments and extracellular polymers (Kraruse et al., 2019).

These results collectively indicate that organo-mineral assemblages formed in MF were enriched in microbially-processed, N-rich OM, linking microbial activity, chemical weathering, and aggregation. Microbes likely accelerated mineral weathering via disaggregation, hydration, and localized dissolution (Banfield et al., 1999; Burghelea et al., 2015; Finlay et al., 2020), releasing Fe and Al that subsequently coprecipitate with, or were sorptively associated with, microbially derived compounds on the surface of cells or biofilms as low-crystallinity Al, Fe, Si mineral phases (Lybrand et al., 2019). This process may have created reactive Fe–Al–OM phases that acted as nucleation sites for aggregation. The observed bacterial community patterns may be linked to these processes. While the community composition differed markedly among the rock treatments, bacterial copy numbers tended to be lower in the basaltic treatments (Table S13) potentially reflecting the protective role of the extractable metal phases. The genus *Neobacillus*, known for its biomineralization potential (Farda et al., 2022; Bhattacharjee et al., 2023), appeared to be enriched in MF relative to the bulk fraction (Fig. 8c), supporting the

idea of MF as a mineralosphere (Uroz et al., 2015) where organo-metallic precipitates and microbial residues interact to drive aggregation.

4.4. Influence of the size and chemical composition of crushed rock

Both particle size and chemistry of the rock materials affected the formation of organo-mineral assemblages. Fine basalt treatment produced significantly more MF than coarse basalt or other treatments (Fig. 3a), emphasizing the importance of mineral particle size in regulating reactivity and aggregation. However, the size effect is not straightforward. Using the basaltic rock from the same source, Yang et al. (2026) observed less formation of Fe_{Ox} and Al_{OX} phases from finer basalt due to greater occlusion of basalt particles within meso-density aggregates, which limited water access and slowed weathering. Thus, multiple factors such as the degree of drying and mixing, OM decomposability, incubation duration, and basalt particle size likely interact to produce size-dependent effects. Even small differences in pore structure or redox dynamics can strongly influence weathering and aggregation, for instance, via affecting Fe-OM interactions (e.g., Chen et al., 2020).

Rock chemistry also influenced OM retention. Despite the similar size distribution (Fig. S2), coarse basalt had greater OM in MF than granite (Fig. 3b), which is attributable to more than one order of magnitude higher initial metal contents, especially in Fe_{OX}, Al_{OX}, and Si_{OX} (Table S2). When normalized to surface area (Table S2), OM accretion in coarse basalt relative to granite corresponds to additional ≈ 0.1 mg C m^{-2}, which lies within sorptive limit of reactive secondary minerals (Wagai and Mayer, 2007; Schneider et al., 2010) and is comparable to C loadings on goethite under in temperate field conditions (Bramble et al., 2024). The strong influence of pre-existing extractable metals (i.e., secondary minerals) in basaltic rock on organo-mineral associations is consistent with findings from a similar incubation experiment (Yang et al., 2026). Although our study lacked fine granite treatment for full factorial comparison, the present results indicate that both particle size and mineralogy jointly regulate organo-mineral assemblage formation and OM stabilization.

4.5. Implications

Our experiment, conducted under simplified conditions, may provide mechanistic insights relevant to early-stage pedogenesis. Weathering of crushed rock in the presence of OM and microbial activity under fluctuating water regimes likely occurs during the early stages of pedogenesis (e.g., primary succession on glacial tills). Although the wet–dry cycles applied here were more intense than typical field conditions, such processes can also occur in agricultural topsoils, where physical mixing and periodic drying can promote mineral–organic interactions. The application of crushed basalt and other mafic rocks to soils has drawn increasing attention as a strategy for CO_2 removal through enhanced weathering (Beerling et al., 2020). Besides CO_2 removal, several pot- and field-scale studies have reported increases in soil OM following mafic rock addition (Buss et al., 2024; Xu et al., 2024), although others found no response (Yan et al., 2023; Sokol et al., 2024). In the current study, we did not detect the significant change in total C possibly due to the short incubation period. Another factor is carbonate formation as the incubation was done under relatively high pH conditions. However, the consistent density-dependent changes in C:N, $\delta^{13}C$, and $\delta^{15}N$ (Fig. 4, section 4.3 above) suggest that total C mainly consists of organic C with minor presence of carbonate. Regardless, our results indicated that the incorporating crushed basalt can promote the formation of stable organo-mineral assemblages via *organo-metallic glue* and thus potentially increase OM persistence. On the other hand, basalt-OM aggregation may reduce the rate of basalt weathering by shielding basalt mineral surfaces from further dissolution, highlighting a possible trade-off between OM stabilization and CO_2 removal efficiency (Yang et al., 2026). Further mechanistic studies are important to better elucidate rock-OM-secondary mineral interactions and to optimize C balance within enhanced rock-weathering strategies.

Across the rock treatments, the degree of OM accretion in MF (fine basalt > coarse basalt > granite > sand, Fig. 3b) corresponded closely to the abundance of reactive Fe_{OX}, Al_{OX}, and Si_{OX} phases from both inherent rock composition (Table S2; Table S10-2) and weathering during incubation (Table S11), suggesting that reactive metal phases controlled OM

retention more strongly than pH (Table 4) or bacterial abundance (Table S13). These results are consistent with the observations at a field scale (e.g., Fukumasu et al., 2021), regional to continental scales (Hughes, 1982; Ashida et al., 2021; von Fromm et al., 2021), up to a global scale (Rasmussen et al., 2018; von Fromm et al., 2025). The current study demonstrated that organo-metallic binding and aggregation can develop rapidly through weathering and microbial processes, directly linking mineral transformation to OM stabilization and highlighting the intimate interactions among microbes, their metabolites, and minerals in soil (Chorover, 2022; Fang et al., 2023; Wagai et al., 2023).

5 Conclusion

The formation of organo-mineral assemblages (meso-density fraction) from the mixture of crushed rocks and leaf compost was observed within 55-day incubation subjected to eight wet-dry cycles. The extent of assemblage formation followed the sequence: fine basalt > coarse basalt > granite ≥ sand. Assemblage development was driven by two coupled processes: (i) microbial transformation of organic matter, evidenced by lower C:N and higher $\delta^{13}C$ and $\delta^{15}N$ relative to the initial leaf compost, and (ii) the supply of reactive Fe and Al, particularly oxalate-extractable Fe, from the rock weathering. The resulting meso-density materials were best characterized as organo-metallic precipitates enriched in oxalate-extractable Fe and, to a less extent, Al phases. These findings provide experimental support for the *organo-metallic glue* hypothesis (Wagai et al., 2020), demonstrating that weathering-derived metals can rapidly induce aggregation and OM persistence. This mechanism links microbial activity, mineral weathering, and OM stabilization, suggesting that early-stage pedogenesis and soil OM formation are strongly controlled by the coupled action of microbial metabolism and reactive metal dynamics.

Data availability. Available upon request.

Supplement. The supplement related to this article is available online.

Author contributions. KM: investigation, methodology, formal analysis, writing (original draft preparation, review, and editing); JJ: investigation; HS: investigation and formal analysis; EM: investigation and formal analysis; RS: investigation and formal analysis; PTY: investigation, formal analysis, and writing (review and editing); RW: conceptualization, methodology, formal analysis, writing (original draft preparation, review and editing), funding acquisition, and supervision.

Competing interests. The authors declare that we have no known competing financial interests or personal relationships that could have appeared to influence the work reported in this paper.

Acknowledgements. The authors are grateful to Y. Yaegaki, R. Hirai, and Y. Yamashita for laboratory assistance; J. Fukumasu for specific surface area analysis; K. Ito for microbial community analysis; and Y. Nakayama for technical advice during the experiment. We also thank M. Bamba, S. Sato, and K. Minamisawa (Tohoku University) for 16S rRNA amplicon sequencing.

Financial support. This paper is based on results obtained from a project, JPNP18016, commissioned by the New Energy and Industrial Technology Development Organization (NEDO).

References

Amelung, W., Tang, N., Siebers, N., Aehnelt, M., Eusterhues, K., Felde, Vi. J. M. N. L., Guggenberger, G., Kaiser, K., Kögel-Knabner, I., Klumpp, E., Knief, C., Kruse, J., Lehndorff, E., Mikutta, R., Peth, S., Ray, N., Prechtel, A., Ritschel,

T., Schweizer, S. A., Woche, S. K., Wu, B., and Totsche, K. U.: Architecture of soil microaggregates: Advanced methodologies to explore properties and functions, Journal of Plant Nutr. Soil Sci., 187, 17–50, 2024.

Angst, G., Messinger, J., Greiner, M., Häusler, W., Hertel, D., Kirfel, K., Kögel-Knabner, I., Leuschner, C., Rethemeyer, J., and Muellera, C.W.: Soil organic carbon stocks in topsoil and subsoil controlled by parent material, carbon input in the rhizosphere, and microbial-derived compounds, Soil Biol. Biochem., 122, 19–30, https://doi.org/10.1016/j.soilbio.2018.03.026, 2018.

Angst, G., Mueller, K. E., Castellano, M. J., Vogel, C., Wiesmeier, M., and Mueller, C. W.: Unlocking complex soil systems as carbon sinks: multi-pool management as the key. Nat. Commun., 14, 2967, https://doi.org/10.1038/s41467-023-38700-5, 2023.

Arai, M., Ikazaki, K., Anzai, T., Celestial, V. P., Tumbay, J. V., Santillana, I. S., and Wagai, R.: Protective role of reactive aluminum phases to stabilize soil organic matter against long-term cultivation in the humid tropics under volcanic influence. Soil Sci. Plant Nutr., 71 (1), 27–37, https://doi.org/10.1080/00380768.2024.2415455, 2025.

Asano, M., and Wagai, R.: Evidence of aggregate hierarchy at micro- to submicron scales in an allophanic Andisol, Geoderma, 216, 62–74, https://doi.org/10.1016/j.geoderma.2013.10.005, 2014.

Ashida, K., Watanabe, T., Urayama, S., Hartono, A., Kilasara, M., Mvondo Ze, A. D., Nakao, A., Sugihara, S., and Funakawa, S.: Quantitative relationship between organic carbon and geochemical properties in tropical surface and subsurface soils, Biogeochemistry, 155, 77–95, https://doi.org/10.1007/s10533-021-00813-8, 2021.

Baldock, J. A., and Skjemstad, J. O.: Role of the soil matrix and minerals in protecting natural organic materials against biological attack, Org. Geochem, 31 (7–8), 697–710, https://doi.org/10.1016/S0146-6380(00)00049-8, 2000.

Bamba, M., Akyol, T. Y., Azuma, Y., Quilbe, J., Andersen, S. U., and Sato, S.: Synergistic effects of plant genotype and soil microbiome on growth in *Lotus japonicus*, FEMS Microbiol. Ecol., 100 (5), fiae056, https://doi.org/10.1093/femsec/fiae056, 2024.

Banfield, J. F., Barker, W. W., Welch, S. A., and Taunton, A.: Biological impact on mineral dissolution: Application of the lichen model to understanding mineral weathering in the rhizosphere, PNAS, 96 (7), 3404–3411, https://doi.org/10.1073/pnas.96.7.3404, 1999.

Basile-Doelsch, I., Balesdent, J., and Rose, J.: Are interactions between organic compounds and nanoscale weathering minerals the key drivers of carbon storage in soils?, Environ. Sci. Technol., 49 (7), 3997−3998, https://doi.org/10.1021/acs.est.5b00650, 2015.

Beerling, D. J., Kantzas, E. P., Lomas, M. R., Wade, P., Eufrasio, R. M., Renforth, P., Sarkar, B., Andrews, M. G., James, R. H., Pearce, C. R., Mercure, J. F., Pollitt, H., Holden, P. B., Edwards, N. R., Khanna, M., Koh, L., Quegan, S., Pidgeon, N. F., Janssens, I. A., Hansen, J., and Banwart, S. A.: Potential for large-scale CO_2 removal via enhanced rock weathering with croplands, Nature, 583, 242–248, https://doi.org/10.1038/s41586-020-2448-9, 2020.

Bhattacharjee, K., Barua, S., Chrungoo, N. K., and Joshi, S. R.: Characterization of biomineralizing and plant growth-promoting attributes of lithobiontic bacteria, Curr. Microbiol., 80, 80, https://doi.org/10.1007/s00284-022-03176-x, 2023.

Bölscher, T., Cardon, Z. G., Garcia Arredondo, M., Grand, S., Griffen, G., Hestrin, R., Imboden, J., Jamoteau, F., Lacroix, E.M., Pérez Castro, S., Persson, P., Riley, W.J., Keiluweit, M.: Vulnerability of mineral-organic associations in the rhizosphere, Nature Comm., 16, https://dx.doi.org/10.1038/s41467-025-61273-4, 2025.

Bramble, D. S. E., Ulrich, S., Schöning, I., Mikutta, R., Brandt, L., Poll, C., Kandeler, E., Mikutta, C., Konrad, A., Siemens, J., Yang, Y., Polle, A., Schall, P., Ammer, C., Kaiser, K., and Schrumpf, M.: Formation of mineral-associated organic matter in temperate soils is primarily controlled by mineral type and modified by land use and management intensity, Glob. Change Biol., 30, e17024, https://doi.org/10.1111/gcb.17024, 2024.

Bucka, F. B., Felde, V. J. M. N. L., Peth, S., and K¨ogel-Knabner, I.: Disentangling the effects of OM quality and soil

texture on microbially mediated structure formation in artificial model soils, Geoderma, 403, 115213, https://doi.org/10.1016/j.geoderma.2021.115213, 2021.

Burghelea, C., Zaharescu, D. G., Dontsova, K., Maier, R., Huxman, T., and Chorover, J.: Mineral nutrient mobilization by plants from rock: Influence of rock type and arbuscular mycorrhiza, Biogeochemistry, 124, 187–203, https://doi.org/10.1007/s10533-015-0092-5, 2015.

Buss, W., Hasemer, H., Ferguson, S., and Borevitz, J.: Stabilisation of soil organic matter with rock dust partially counteracted by plants, Glob. Chang. Biol., 30 (1), e17052, https://doi.org/10.1111/gcb.17052, 2024.

Chapman, J. B., Weiss, D. J., Shan, Y., and Lemburger, M.: Iron isotope fractionation during leaching of granite and basalt by hydrochloric and oxalic acids, Geochim. Cosmochim. Acta, 73 (5), 1312–1324, https://doi.org/10.1016/j.gca.2008.11.037, 2009.

Chen, C., Dynes, J. J., Wang, J., Karunakaran, C., and Sparks, D. L.: Soft X-ray spectromicroscopy study of mineral-organic matter associations in pasture soil clay fractions, Environ. Sci. Technol., 48 (12), 6678–6686, https://doi.org/10.1021/es405485a, 2014.

Chen, C., Hall, S. J., Coward, E., and Thompson, A.: Iron-mediated organic matter decomposition in humid soils can counteract protection, Nat. Commun., 11, 2255, https://doi.org/10.1038/s41467-020-16071-5, 2020.

Choi, W. J., Kwak, J. H., Park, H. J., Yang, H. I., Park, S. I., Xu, Z., Lee, S. M., Lim, S. S., and Chang S. X.: Land-use type, and land management and disturbance affect soil $\delta^{15}N$: A review, J. Soils Sediments, 20, 3283–3299, https://doi.org/10.1007/s11368-020-02708-x, 2020.

Chorover, J.: Microbe-biomolecule-mineral interfacial reactions, in: Multi-Scale Biogeochemical Processes in Soil Ecosystems: Critical Reactions and Resilience to Climate Changes, edited by: Yang, Y., Keiluweit, M., Senesi, N., and Xing, B., John Wiley & Sons, Inc., Hoboken, 117–140, https://doi.org/10.1002/9781119480419, 2022.

Cole, J. R., Wang, Q., Fish, J. A., Chai, B., McGarrell, D. M., Sun, Y., Brown, C. T., Porras-Alfaro, A., Kuske, C. R., and Tiedje, J. M.: Ribosomal Database Project: Data and tools for high throughput rRNA analysis, Nucleic Acids Res., 42 (D1), D633–D642, https://doi.org/10.1093/nar/gkt1244, 2014.

Cornell, R. M., and Schwertmann, U. (Eds.): The Iron Oxides: Structure, Properties, Reactions, Occurences and Uses, Wiley-VCH Verlag GmbH & Co. KGaA, ISBN9783527602094, 2003.

Edgar, R. C.: SINTAX: A simple non-Bayesian taxonomy classifier for 16S and ITS sequences, bioRxiv, 074161, https://doi.org/10.1101/074161, 2016.

Fang, Q., Lu, A., Hong, H., Kuzyakov, Y., Algeo, T. J., Zhao, L., Olshansky, Y., Moravec, B., Barrientes, D. M., and Chorover, J.: Mineral weathering is linked to microbial priming in the critical zone, Nat. Commun., 14, 345, https://doi.org/10.1038/s41467-022-35671-x, 2023.

Farda, B., Djebaili, R., Del Gallo, M., Ercole, C., Bellatreccia, F., and Pellegrini, M.: The “Infernaccio” gorges: Microbial diversity of black deposits and isolation of manganese-solubilizing bacteria, Biol., 11 (8), 1204, https://doi.org/10.3390/biology11081204, 2022.

Finlay, R. D., Mahmood, S., Rosenstock, N., Bolou-Bi, E. B., Köhler, S. J., Fahad, Z. Rosling, A., Wallander, H., Belyazid, S., Bishop, K., and Lian, B.: Reviews and syntheses: Biological weathering and its consequences at different spatial levels – from nanoscale to global scale, Biogeosciences, 17 (6), 1507–1533, https://doi.org/10.5194/bg-17-1507-2020, 2020.

Friedlingstein, P., O'Sullivan, M., Jones, M. W., Andrew, R. M., Gregor, L., Hauck, J., Quéré, C. Le, Luijkx, I. T., Olsen, A., and Peters, G. P., et al.: Global Carbon Budget 2022, Earth Syst. Sci. Data, 14, 4811–4900, https://doi.org/10.5194/essd-14-4811-2022, 2022.

Fukumasu, J., Poeplau, C., Coucheney, E., Jarvis, N., Kl¨offel, T., Koestel, J., K¨atterer, T., Svensson, D. N., Wetterlind, J., and Larsbo, M.: Oxalate-extractable aluminum alongside carbon inputs may be a major determinant for organic carbon content in agricultural topsoils in humid continental climate, Geoderma, 402, 115345,

https://doi.org/10.1016/j.geoderma.2021.115345, 2021.

Fukumasu, J., Yang, P. T., Kajiura, M., Gregorich, E., and Wagai, R.: Soil extraction with pyrophosphate-dithionite mixture: a practical method to estimate organic carbon associated with metal cations and reactive mineral phases, Soil Sci. Plant Nutr., 1–13, https://doi.org/10.1080/00380768.2024.2448861, 2025.

Golchin, A., Oades, J. M., Skjemstad, J. O., and Clarke, P.: Study of free and occluded particulate organic matter in soils by solid state ^{13}C Cp/MAS NMR spectroscopy and scanning electron microscopy, Aust. J. Soil Res., 32 (2), 285–309, https://doi.org/10.1071/SR9940285, 1994.

Goslee, S. C., and Urban, D. L.: The ecodist package for dissimilarity-based analysis of ecological data, J. Stat. Softw., 22 (7), 1–19, https://doi.org/10.18637/jss.v022.i07, 2007.

Gray, J., and Murphy, B.: Parent material and world soil distribution, in: Symposium no. 21, Proceedings of 17th World Congress of Soil Science, 2215, 1–14, 2002.

Hall, S. J., Ye, C., Weintraub, S. R., and Hockaday, W. C.: Molecular trade-offs in soil organic carbon composition at continental scale, Nat. Geosci., 13, 687–692, https://doi.org/10.1038/s41561-020-0634-x, 2020.

Hall, S. J., and Thompson, A.: What do relationships between extractable metals and soil organic carbon concentrations mean?, Soil Sci. Soc. Am. J., 86, 195–208, https://doi.org/10.1002/saj2.20343, 2022.

Hara, S., Kakizaki, K., Bamba, M., Itakura, M., Sugawara, M., Suzuki, A., Sasaki, Y., Takeda, M., Tago, K., Ohbayashi, T., Aono, T., Aoyagi, L. N., Shimada, H., Shingubara, R., Masuda, S., Shibata, A., Shirasu, K., Wagai, R., Akiyama, H., Sato, S., and Minamisawa, K.: Does rhizobial inoculation change the microbial community in field soils? A comparison with agricultural land-use changes, Microbes Environ., 39 (3), ME24006, https://doi.org/10.1264/jsme2.ME24006, 2024.

Harter, R. D., and Naidu, R.: Role of metal-organic complexation in metal sorption by soils, Adv. Agron., 55, 219–263, https://doi.org/10.1016/S0065-2113(08)60541-6, 1995.

Hartmann, M., and Six, J.: Soil structure and microbiome functions in agroecosystems, Nat. Rev. Earth Environ., 4, 4–18, https://doi.org/10.1038/s43017-022-00366-w, 2023.

Hatton, P. J., Kleber, M., Zeller, B., Moni, C., Plante, A. F., Townsend, K., Gelhaye, L., Lajtha, K., and Derrien, D.: Transfer of litter-derived N to soil mineral-organic associations: Evidence from decadal ^{15}N tracer experiments, Org. Geochem., 42 (12), 1489–1501, https://doi.org/10.1016/j.orggeochem.2011.05.002, 2012.

Heckman, K., Lawrence, C. R., and Harden, J. W.: A sequential selective dissolution method to quantify storage and stability of organic carbon associated with Al and Fe hydroxide phases, Geoderma, 312, 24–35, https://doi.org/10.1016/j.geoderma.2017.09.043, 2018.

Heckman, K., Hicks Pries, C. E., Lawrence, C. R., Rasmussen, C., Crow, S. E., Hoyt, A. M., von Fromm, S. F., Shi, Z., Stoner, S., McGrath, C., Beem-Miller, J., Berhe, A. A., Blankinship, J. C., Keiluweit, M., Marín-Spiotta, E., Monroe, J. G., Plante, A. F., Schimel, J., Sierra, C. A., Thompson, A., and Wagai, R.: Beyond bulk: Density fractions explain heterogeneity in global soil carbon abundance and persistence, Glob. Chang Biol., 28 (3), 1178–1196, https://doi.org/10.1111/gcb.16023, 2022.

Hemingway, J. D., Rothman, D. H., Grant, K. E., Rosengard, S. Z., Eglinton, T. I., Derry, L. A., and Galy, V. V.: Mineral protection regulates long-term global preservation of natural organic carbon, Nature, 570, 228–231, https://doi.org/10.1038/s41586-019-1280-6, 2019.

Hiradate, S., Nakadai, T., Shindo, H., and Yoneyama, T.: Carbon source of humic substances in some Japanese volcanic ash soils determined by carbon stable isotopic ratio, $\delta^{13}C$, Geoderma, 119 (1–2), 133–141, https://doi.org/10.1016/S0016-7061(03)00257-X, 2004.

Hitchcock, A. P.: aXis 2000 - Analysis of X-ray Images and Spectra, http://unicorn.mcmaster.ca/aXis2000.html, 2023.

Horie, Y., Iwasaki, A., Tomoyose, N., Kido, M., Yamaguchi, T., Tada, K., Kawashita, H., Kohno, A., Hamamura, K., Yamazoe, R., Matsumoto, R., Yokoyama, S., Noguchi, I., Yagoh, H., Kai, I., Hamano, A., and Yoshida, F.: Acid

deposition survey in Japan, phase 5 (2016). Journal of Environmental Laboratories Association, 41 (3), 2–37, http://db.cger.nies.go.jp/dataset/acidrain/ja/05/, 2016. (in Japanese).

Hughes, J. C.: High gradient magnetic separation of some soil clays from Nigeria, Brazil and Colombia. I. The interrelationships of iron and aluminium extracted by acid ammonium oxalate and carbon. Eur. J. Soil Sci., 33, 509–519, https://doi.org/10.1111/j.1365-2389.1982.tb01785.x, 1982.

IUSS Working Group WRB (Eds.): World Reference Base for Soil Resources 2014, update 2015: International soil classification system for naming soils and creating legends for soil maps, World Soil Resources Reports No. 106, FAO, Rome, 2015.

Jamoteau, F., Cam, N., Levard, C., Doelsch, E., Gassier, G., Duvivier, A., Boulineau, A., Saint-Antonin, F., and Basile-Doelsch, I.: Structure and chemical composition of soil C-rich Al−Si−Fe coprecipitates at nanometer scale, Environ. Sci. Technol., 57 (49), 20615−20626, https://doi.org/10.1021/acs.est.3c06557, 2023.

Jamoteau, F., Doelsch, E., Cam, N., Levard, C., Woignier, T., Boulineau, A., Saint-Antonin, F., Swaraj, S., Gassier, G., Duvivier, A., Borschneck, D., Pons, M-L., Chaurand, P., Vidal, V., Brouilly, N., and Basile-Doelsch, I.: Interplay of coprecipitation and adsorption processes: deciphering amorphous mineral–organic associations under both forest and cropland conditions, SOIL, 11 (2), 535–552, https://doi.org/10.5194/soil-11-535-2025, 2025.

Kaiser, K., Guggenberger, G., Haumaier, L., and Zech, W.: Dissolved organic matter sorption on subsoils and minerals studied by ^{13}C-NMR and DRIFT spectroscopy. Eur. J. Soil Sci. 48 (2), 301–310, https://doi.org/10.1111/j.1365-2389.1997.tb00550.x, 1997.

Keil, R. G., and Mayer, L. M.: Mineral matrices and organic matter, in: Treatise on Geochemistry (Second Edition), edited by: Holland, H. D., and Turekian, K. K., Elsevier, 337–359, https://doi.org/10.1016/B978-0-08-095975-7.01024-X, 2014.

Kleber, M., Eusterhues, K., Keiluweit, M., Mikutta, C., Mikutta, R., and Nico, P. S.: Chapter one - mineral–organic associations: Formation, properties, and relevance in soil environments, in: Advances in Agronomy, edited by: Sparks, D. L., Academic Press, Volume 130, 1–140, https://doi.org/10.1016/bs.agron.2014.10.005, 2015.

Koba, K., Kinoshita, K., Onishi, Y., Fukushima, K., Osaka, K., Matsuo, N., Funakawa, K., Seko, Y., Medo, A., Hirasawa, R., O Ogawa, N., Hyodo, F., and Yoshimizu, C.: Carbon and nitrogen isotope analysis on small samples using a near-conventional EA-IRMS system, Radioisotopes, 70 (4), 291–299, https://doi.org/10.3769/radioisotopes.70.291, 2021. (in Japanese).

Krause, L., Biesgen, D., Treder, A., Schweizer, S. A., Klumpp, E., Knief, C., and Siebers, N.: Initial microaggregate formation: Association of microorganisms to montmorillonite-goethite aggregates under wetting and drying cycles, Geoderma, 351, 250–260, https://doi.org/10.1016/j.geoderma.2019.05.001, 2019.

Lawrence, C. R., Harden, J. W., Xu, X., Schulz, M. S., and Trumbore, S. E.: Long-term controls on soil organic carbon with depth and time: A case study from the Cowlitz River Chronosequence, WA USA, Geoderma, 247–248, 73–87, https://doi.org/10.1016/j.geoderma.2015.02.005, 2015.

Lehmann, J., Bossio, D. A., Kögel-Knabner, I., and Rillig, M. C.: The concept and future prospects of soil health, Nat. Rev. Earth Environ., 1, 544–553, https://doi.org/10.1038/s43017-020-0080-8, 2020.

Liu, C., Cui, Y., Li, X., and Yao, M.: microeco: an R package for data mining in microbial community ecology, FEMS Microbiol. Ecol., 97 (2), fiaa255, https://doi.org/10.1093/femsec/fiaa255, 2021.

Lundström, U. S., van Breemen, N., and Bain, D.: The podzolization process. A review, Geoderma, 94 (2–4), 91–107, https://doi.org/10.1016/S0016-7061(99)00036-1, 2000.

Lybrand, R. A., Austin, J. C., Fedenko, J., Gallery, R. E., Rooney, E., Schroeder, P. A., Zaharescu, D. G., and Qafoku, O.: A coupled microscopy approach to assess the nano-landscape of weathering, Sci. Rep., 9, 5377, https://doi.org/10.1038/s41598-019-41357-0, 2019.

Mao, X., Van Zwieten, L., Zhang, M., Qiu, Z., Yao, Y., and Wang., H.: Soil parent material controls organic matter stocks

and retention patterns in subtropical China, J. Soils Sediments, 20, 2426–2438, https://doi.org/10.1007/s11368-020-02578-3, 2020.

Martinelli, L. A., Piccolo, M. C., Townsend, A. R., Vitousek, P. M., Cuevas, E., McDowell, W., Robertson, G. P., Santos, O. C., and Treseder, K.: Nitrogen stable isotopic composition of leaves and soil: Tropical versus temperate forests, Biogeochemistry, 46, 45–65, https://doi.org/10.1007/BF01007573, 1999.

Masiello, C. A., Chadwick, O. A., Southon, J., Torn, M. S., and Harden, J. W.: Weathering controls on mechanisms of carbon storage in grassland soils, Global Biogeochem. Cycles, 18, GB4023, https://doi.org/10.1029/2004GB002219, 2004.

McMurdie, P. J., and Holmes, S.: phyloseq: An R package for reproducible interactive analysis and graphics of microbiome census data, PLoS ONE, 8 (4), e61217, https://doi.org/10.1371/journal.pone.0061217, 2013.

Moni, C., Derrien, D., Hatton, P. J., Zeller, B., and Kleber, M.: Density fractions versus size separates: Does physical fractionation isolate functional soil compartments?, Biogeosciences, 9 (12), 5181–5197, https://doi.org/10.5194/bg-9-5181-2012, 2012.

Oades, J.M. The retention of organic matter in soils. Vol. 5 Issue 1 Pages 35-70, https://doi.org/ 10.1007/BF02180317, Biogeochemistry, 1988.

Ogawa, N. O., Nagata, T., Kitazato, H., and Ohkouchi, N.: Ultra-sensitive elemental analyzer/isotope ratio mass spectrometer for stable nitrogen and carbon isotope analyses, in: Earth, Life and Isotopes, edited by: Ohkouchi, N., Tayasu, I., and Koba, K., Kyoto University Press, Kyoto, Japan, 339–353. ISBN: 9784876989607, 2010.

Oksanen, J.: Vegan: ecological diversity. R project, 368, 1–11, https://cran.r-project.org/web/packages/vegan/vignettes/diversity-vegan.pdf, 2013.

Orgill, S. E., Condon, J. R., Conyers, M. K., Morris, S. G., Murphy, B. W., and Greene, R. S. B.: Parent material and climate affect soil organic carbon fractions under pastures in south-eastern Australia, Soil Res., 55 (8), 799–808, https://doi.org/10.1071/SR16305, 2017.

Parker, D. R.: Aluminum speciation, in: Encyclopedia of Soils in the Environment, edited by: Hillel, D., Elsevier, 50–56, https://doi.org/10.1016/B0-12-348530-4/00199-5, 2005.

Percival, H. J., Parfitt, R. L., and Scott, N. A.: Factors controlling soil carbon levels in New Zealand grasslands is clay content important?, Soil Sci. Soc. Am. J., 64 (5), 1623–1630, https://doi.org/10.2136/sssaj2000.6451623x, 2000.

Philippot, L., Chenu, C., Kappler, A., Rillig, M. C., and Fierer, N.: The interplay between microbial communities and soil properties, Nat. Rev. Microbiol., 22, 226–239, https://doi.org/10.1038/s41579-023-00980-5, 2024.

Possinger, A. R., Zachman, M. J., Enders, A., Levin, B. D. A., Muller, D. A., Kourkoutis, L. F., and Lehmann, J.: Organo–organic and organo–mineral interfaces in soil at the nanometer scale, Nat. Commun., 11, 6103, https://doi.org/10.1038/s41467-020-19792-9, 2020.

Prietzel, J., Müller, S., Kögel-Knabner, I., Thieme, J., Jaye, C., and Fischer, D.: Comparison of soil organic carbon speciation using C NEXAFS and CPMAS ^{13}C NMR spectroscopy, Sci. Total Environ., 628–629, 906–918, https://doi.org/10.1016/j.scitotenv.2018.02.121, 2018.

Pronk, G. J., Heister, K., Vogel, C., Babin, D., Bachmann, J., Ding, G. C., Ditterich, F., Gerzabek, M. H., Giebler, J., Hemkemeyer, M., Kandeler, E., Mouvenchery, Y. K., Miltner, A., Poll, C., Schaumann, G. E., Smalla, K., Steinbach, A., Tanuwidjaja, I., Tebbe, C. C., Wick, L. Y., Woche, S. K., Totsche, K. U., Schloter, M., and Kögel-Knabner, I.: Interaction of minerals, organic matter, and microorganisms during biogeochemical interface formation as shown by a series of artificial soil experiments, Biol. Fertil. Soils, 53, 9–22, https://doi.org/10.1007/s00374-016-1161-1, 2017.

Rabot, E., Wiesmeier, M., Schlüter, S., and Vogel, H. -J.: Soil structure as an indicator of soil functions: A review, Geoderma, 314, 122–137, https://doi.org/10.1016/j.geoderma.2017.11.009, 2018.

Rasmussen, C., Heckman, K., Wieder, W. R., Keiluweit, M., Lawrence, C. R., Berhe, A. A., Blankinship, J. C., Crow, S. E.,

Druhan, J. L., and Pries, C. E. H. et al.: Beyond clay: towards an improved set of variables for predicting soil organic matter content, Biogeochemistry, 137, 297–306, https://doi.org/10.1007/s10533-018-0424-3, 2018.

Rasmussen, C., Torn, M. S., and Southard, R. J.: Mineral assemblage and aggregates control carbon dynamics in a California conifer forest, Soil Sci. Soc. Am. J., 69 (6), 1711–1721, https://doi.org/10.2136/sssaj2005.0040, 2005.

Regelink, I. C., Stoof, C. R., Rousseva, S., Weng, L., Lair, G. J., Kram, P., Nikolaidis, N. P., Kercheva, M., Banwart, S., and Comans, R. N. J.: Linkages between aggregate formation, porosity and soil chemical properties, Geoderma, 247–248, 24–37, https://doi.org/10.1016/j.geoderma.2015.01.022, 2015.

Rennert, T.: Wet-chemical extractions to characterise pedogenic Al and Fe species – a critical review, Soil Res., 57, 1–16, https://doi.org/10.1071/SR18299, 2019.

Rowley, M. C., Nico, P. S., Bone, S. E., Marcus, M. A., Pegoraro, E. F., Castanha, C., Kang, K., Bhattacharyya, A., and Torn, M. S.: Association between soil organic carbon and calcium in acidic grassland soils from Point Reyes National Seashore, CAPeña, Jasquelin, Biogeochemistry, 165, 91–111, https://doi.org/10.1007/s10533-023-01059-2, 2023.

Saidy, A. R., Smernik, R. J., Baldock, J. A., Kaiser, K., and Sanderman, J.: Microbial degradation of organic carbon sorbed to phyllosilicate clays with and without hydrous iron oxide coating, Eur. J. Soil Sci., 66 (1), 83–94, https://doi.org/10.1111/ejss.12180, 2015.

Schneider, M. P. W., Scheel, T., Mikutta, R., van Hees, P., Kaiser, K., and Kalbitz, K.: Sorptive stabilization of organic matter by amorphous Al hydroxide, Geochim. Cosmochim. Acta, 74, 1606–1619, https://doi.org/10.1016/j.gca.2009.12.017, 2010.

Shang, C., and Tiessen, H.: Organic matter stabilization in two semiarid tropical soils: Size, density, and magnetic separations, Soil Sci. Soc. Am. J., 62 (5), 1247–1257, https://doi.org/10.2136/sssaj1998.03615995006200050015x, 1998.

Shimada, H., Wagai, R., Inoue, Y., Tamura, K., and Asano, M.: Millennium timescale carbon stability in an Andisol: How persistent are organo-metal complexes?, Geoderma, 417, 115820, https://doi.org/10.1016/j.geoderma.2022.115820, 2022.

Soil Survey Staff. (Eds.): Keys to Soil Taxonomy, 12th ed, USDA-Natural Resources Conservation Service, Washington, DC, 2014.

Sokol, N. W., Sohng, J., Moreland, K., Slessarev, E., Goertzen, H., Schmidt, R., Samaddar, S., Holzer, I., Almaraz, M., Geoghegan, E., Houlton, B., Montañez, I., Pett-Ridge, J., and Scow, K.: Reduced accrual of mineral-associated organic matter after two years of enhanced rock weathering in cropland soils, though no net losses of soil organic carbon, Biogeochemistry, 167, 989–1005, https://doi.org/10.1007/s10533-024-01160-0, 2024.

Sollins, P., Homann, P., and Caldwell, B. A.: Stabilization and destabilization of soil organic matter: mechanisms and controls, Geoderma, 74 (1–2), 65–105, https://doi.org/10.1016/S0016-7061(96)00036-5, 1996.

Sollins, P., Kramer, M. G., Swanston, C., Lajtha, K., Filley, T., Aufdenkampe, A. K., Wagai, R., and Bowden, R. D.: Sequential density fractionation across soils of contrasting mineralogy: Evidence for both microbial- and mineral-controlled soil organic matter stabilization, Biogeochemistry, 96, 209–231, https://doi.org/10.1007/s10533-009-9359-z, 2009.

Solomon, D., Lehmann, J., Harden, J., Wang, J., Kinyangi, J., Heymann, K., Karunakaran, C., Lu, Y., Wirick, S., and Jacobsen, C.: Micro- and nano-environments of carbon sequestration: Multi-element STXM–NEXAFS spectromicroscopy assessment of microbial carbon and mineral associations, Chem. Geol., 329, 53–73, https://doi.org/10.1016/j.chemgeo.2012.02.002, 2012.

Sørensen, L. H.: Stabilization of newly formed amino acid metabolites in soil by clay minerals, Soil Sci., 114 (1), 5–11, https://doi.org/10.1097/00010694-197207000-00002, 1972.

Suzuki, M. T., Taylor, L. T., and DeLong, E. F.: Quantitative analysis of small-subunit rRNA genes in mixed microbial populations via 5′-nuclease assays. Appl. Environ. Microbiol., 66 (11), 4605–4614, https://doi.org/10.1128/AEM.66.11.4605-4614.2000, 2000.

Takahashi, T., and Dahlgren, R. A.: Nature, properties and function of aluminum–humus complexes in volcanic soils, Geoderma, 263, 110–121, https://doi.org/10.1016/j.geoderma.2015.08.032, 2016.

Takeichi, Y., Inami, N., Suga, H., Miyamoto, C., Ueno, T., Mase, K., Takahashi, Y., and Ono, K.: Design and performance of a compact scanning transmission X-ray microscope at the Photon Factory, Rev. Sci. Instrum., 87 (1), 013704, https://doi.org/10.1063/1.4940409, 2016.

Tamrat, W. Z., Rose, J., Grauby, O., Doelsch, E., Levard, C., Chaurand, P., and Basile-Doelsch, I.: Composition and molecular scale structure of nanophases formed by precipitation of biotite weathering products, Geochim. Cosmochim. Acta, 229, 53–64, https://doi.org/10.1016/j.gca.2018.03.012, 2018.

Tamrat, W. Z., Rose, J., Grauby, O., Doelsch, E., Levard, C., Chaurand, P., and Basile-Doelsch, I.: Soil organo-mineral associations formed by co-precipitation of Fe, Si and Al in presence of organicligands, Geochim. Cosmochim. Acta, 260, 15–28, https://doi.org/10.1016/j.gca.2019.05.043, 2019.

Tipping, E.: The adsorption of aquatic humic substances by iron oxides, Geochim. Cosmochim. Acta, 45 (2), 191–199, https://doi.org/10.1016/0016-7037(81)90162-9, 1981.

Torn, M. S., Trumbore, S. E., Chadwick, O. A., Vitousek, P. M., and Hendricks, D. M.: Mineral control of soil organic carbon storage and turnover, Nature, 389, 170–173, https://doi.org/10.1038/38260, 1997.

Totsche, K. U., Amelung, W., Gerzabek, M. H., Guggenberger, G., Klumpp, E., Knief, C., Lehndorff, E., Mikutta, R., Peth, S., Prechtel, A., Ray, N., and Kögel-Knabner, I.: Microaggregates in soils, J. Plant Nutr. Soil Sci., 181, 104–136, https://doi.org/10.1002/jpln.201600451, 2018.

Underwood, T. R., Bourg, I. C., and Rosso, K. M.: Mineral-associated organic matter is heterogeneous andstructured by hydrophobic, charged, and polar interactions, PNAS, 121 (46), e2413216121, https://doi.org/10.1073/pnas.2413216121, 2024.

Uroz, S., Kelly, L. C., Turpault, M. P., Lepleux, C., and Frey-Klett, P.: The mineralosphere concept: Mineralogical control of the distribution and function of mineral-associated bacterial communities, Trends Microbiol., 23 (12), 751–762, https://doi.org/10.1016/j.tim.2015.10.004, 2015.

Vogel, C., Babin, D., Pronk, G. J., Heister, K., Smalla, K., and Kögel-Knabner, I.: Establishment of macro-aggregates and organic matter turnover by microbial communities in long-term incubated artificial soils, Soil Biol. Biochem., 79, 57–67, https://doi.org/10.1016/j.soilbio.2014.07.012, 2014.

von Fromm, S. F., Hoyt, A. M., Lange, M., Acquah, G. E., Aynekulu, E., Berhe, A. A., Haefele, S. M., McGrath, S. P., Shepherd, K. D., Sila, A. M., Six, J., Towett, E. K., Trumbore, S. E., Vågen, T.-G., Weullow, E., Winowiecki, L. A., and Doetterl, S.: Continental-scale controls on soil organic carbon across sub-Saharan Africa, SOIL, 7, 305–332, https://doi.org/10.5194/soil-7-305-2021, 2021.

von Fromm, S. F., Jungkunst, H. F., Amenkhienan, B., Hall, S. J., Georgiou, K., Pries, C. H., Montaño-López, F., Quesada, C. A., Rasmussen, C., Schrumpf, M., Singh, B., Thompson, A., Wagai, R., and Fiedler, S.: Moisture and soil depth govern relationships between soil organic carbon and oxalate-extractable metals at the global scale, Biogeochemistry, 168, 20, https://doi.org/10.1007/s10533-025-01208-9, 2025.

Wagai, R., and Sollins, P.: Biodegradation and regeneration of water-soluble carbon in a forest soil: Leaching column study, Biol. Fertil. Soils, 35, 18–26, https://doi.org/10.1007/s00374-001-0434-4, 2002.

Wagai, R., and Mayer, L.M.: Sorptive stabilization of organic matter in soils by hydrous iron oxides, Geochim. Cosmochim. Acta, 71 (1), 25–35, https://doi.org/10.1016/j.gca.2006.08.047, 2007.

Wagai, R., Kishimoto-Mo, A. W., Yonemura, S., Shirato, Y., Hiradate, S., and Yagasaki, Y.: Linking temperature sensitivity of soil organic matter decomposition to its molecular structure, accessibility, and microbial physiology, Glob. Chang. Biol., 19 (4), 1114–1125, https://doi.org/10.1111/gcb.12112, 2013a.

Wagai, R., Mayer, L. M., Kitayama, K., and Shirato, Y.: Association of organic matter with iron and aluminum across a

range of soils determined via selective dissolution techniques coupled with dissolved nitrogen analysis, Biogeochemistry, 112, 95–109, https://doi.org/10.1007/s10533-011-9652-5, 2013b.

Wagai, R., Kajiura, M., Asano, M., and Hiradate, S.: Nature of soil organo-mineral assemblage examined by sequential density fractionation with and without sonication: Is allophanic soil different?, Geoderma, 241–242, 295–305, https://doi.org/10.1016/j.geoderma.2014.11.028, 2015.

Wagai, R., Kajiura, M., Uchida, M., and Asano, M.: Distinctive roles of two aggregate binding agents in allophanic Andisols: Young carbon and poorly-crystalline metal phases with old carbon, Soil Syst., 2 (2), 29, https://doi.org/10.3390/soilsystems2020029, 2018.

Wagai, R., Kajiura, M., and Asano, M.: Iron and aluminum association with microbially processed organic matter via meso-density aggregate formation across soils: Organo-metallic glue hypothesis, SOIL, 6 (2), 597–627, https://doi.org/10.5194/soil-6-597-2020, 2020.

Wagai, R., Yang, P. T., and Kaiser, K.: Interfacial reactions of microorganisms with minerals and organic matter, in: Encyclopedia of Soils in the Environment (Second Edition), edited by: Goss, M. J., and Oliver, M., Academic Press, 458–469, https://doi.org/10.1016/B978-0-12-822974-3.00232-9, 2023.

Wan, J., Tyliszczak, T., and Tokunaga, T. K.: Organic carbon distribution, speciation, and elemental correlations within soil microaggregates: Applications of STXM and NEXAFS spectroscopy, Geochim. Cosmochim. Acta, 71 (22), 5439–5449, https://doi.org/10.1016/j.gca.2007.07.030, 2007.

Watanabe, T., Harsh, J. B., and Wagai, R.: Short-range ordered aluminosilicates, in: Encyclopedia of Soils in the Environment (Second Edition), edited by: Goss, M. J., and Oliver, M., Academic Press, 121–134, https://doi.org/10.1016/B978-0-12-822974-3.00223-8, 2023.

Wattel-Koekkoek, E. J. W., Buurman, P., Van der Plicht, J., Wattel, E., and Van Breemen, N.: Mean residence time of soil organic matter associated with kaolinite and smectite, Eur. J. Soil Sci., 54 (2), 269–278, https://doi.org/10.1046/j.1365-2389.2003.00512.x, 2003.

Xu, T., Yuan, Z., Vicca, S., Goll, D. S., Li, G., Lin, L., Chen, H., Bi, B., Chen, Q., Li, C., Wang, X., Wang, C., Hao, Z., Fang, Y., and Beerling, D. J.: Enhanced silicate weathering accelerates forest carbon sequestration by stimulating the soil mineral carbon pump, Glob. Change Biol., 30 (8), e17464, https://doi.org/10.1111/gcb.17464, 2024.

Yan, Y., Dong, X., Li, R., Zhang, Y., Yan, S., Guan, X., Yang, Q., Chen, L., Fang, Y., Zhang, W., and Wang, S.: Wollastonite addition stimulates soil organic carbon mineralization: Evidences from 12 land-use types in subtropical China, Catena, 225, 107031, https://doi.org/10.1016/j.catena.2023.107031, 2023.

Yang, P. T., Kurokawa, K., Nakao, A., Matsumura, E., and Wagai, R.: The potential of enhanced rock weathering for CO_2 removal and soil organic carbon storage via organo-mineral aggregation: the trade-off induced by basaltic rock particle size. Biogeochemistry, 169, 9, https://doi.org/10.1007/s10533-025-01296-7, 2026.

Yudina, A., and Kuzyakov, Y.: Dual nature of soil structure: The unity of aggregates and pores, Geoderma, 434, 116478, https://doi.org/10.1016/j.geoderma.2023.116478, 2023.